Theoretical development and first-principles analysis of strongly correlated systems

by

Chen Liu

A dissertation submitted to the graduate faculty

in partial fulfillment of the requirements for the degree of

DOCTOR OF PHILOSOPHY

Major: Condensed Matter Physics

Program of Study Committee:

Kai-Ming Ho, Major Professor

James Evans

Xueyu Song

German Valencia

Edward Yu

Iowa State University

Ames, Iowa

2016

Copyright © Chen Liu, 2016. All rights reserved.

TABLE OF CONTENTS

LIST OF TABLES v

LIST OF FIGURES vi

ACKNOWLEDGEMENTS x

CHAPTER 1. INTRODUCTION 1

CHAPTER 2. METHODS IN MANY-BODY QUANTUM THEORY . 5

2.1 Many-body Hamiltonian 5

2.2 Hartree-Fock approximation 6

2.3 Density functional theory 8

2.4 Basic machinery for solving self-consistent equations 11

2.5 Basis sets in molecular systems 13

2.6 Basis sets in periodic materials 15

2.6.1 Plane waves and pseudopotential 15

2.6.2 LAPW methods 16

CHAPTER 3. CORRELATION MATRIX RENORMALIZATION THEORY 19

3.1 Introduction 19

3.2 Second quantization 21

3.2.1 First quantization 21

3.2.2 Basic concepts of second quantization 22

3.2.3 Mean-field theory and Hartree-Fock approximation 23

3.3 CMR formalism 24
3.4 Reducing errors introduced by CMR approximation 29
3.4.1 Analytical expression for H_2 with minimal basis 30
3.4.2 The form of z-factor and sum rules 33
3.5 Construction of quasi-atomic minimal-basis-set orbitals 35
3.6 Self-consistent loop 40
3.7 Results and discussions 40
3.7.1 Hydrogen clusters 41
3.7.2 Large basis through QUAMBO approach 45
3.7.3 Molecules with multiple active orbitals 46
CHAPTER 4. COUPLING CONSTANT INTEGRATION METHOD FOR TOTAL ENERGY CALCULATION 49
4.1 Introduction 49
4.2 Magnetic anisotropy energy 51
4.3 Formulation 52
4.3.1 Total energy and MAE from CCI 52
4.3.2 Decomposition of SOC energy 54
4.4 Results and discussions 55
4.4.1 Total energy from CCI 55
4.4.2 MAE from CCI 56
4.4.3 Decomposition of E^{SO} 59
CHAPTER 5. INVESTIGATION OF GROUND STATE TRANSITION IN $CaIrO_3$ BY DFT+DMFT 61
5.1 Introduction 61
5.2 A combination of the DFT and DMFT 62
5.3 Computational details of the DFT+DMFT calculation 66
5.4 Results and discussions 69

CHAPTER 6. CONCLUSION 76

BIBLIOGRAPHY 78

LIST OF TABLES

Table 3.1 Summary of equilibrium bond length R_e and binding energy E_b for a series of molecules. QUAMBO-FCI, QUAMBO-CMR and experimental data [1, 2] are included. 47

Table 4.1 Comparison of the total energy change, calculated from the CCI and from the SCC. 56

Table 4.2 Comparison of the MAE per formula unit for FePt and CoPt calculated from two methods. The MAE with its relative errors from the CCI method is also listed according to three different numbers of data points. 58

Table 4.3 Decomposition of spin-orbit coupling energy E_{SO}(meV) and orbital magnetic moment $M_l(m\mu_B)$ into different atomic sites and spin components. The anisotropies of E_{SO} and M_l for two different orientations are defined as $K_{SO} = E^x_{SO} - E^z_{SO}$ and $K_l = M^z_l - M^x_l$. 59

LIST OF FIGURES

Figure 2.1 Flow chart of self-consistent procedure in solving KS equations. . 12

Figure 2.2 Sketch of muffin-tin (S) and interstitial (I) regions in a unit cell. 17

Figure 3.1 Flow chart of the CMR program with sum-rule terms through the approach of QUAMBO. The orange boxes are also self-consistent loops inside for solving the single-particle equations and local configurations. 41

Figure 3.2 Potential energy curve and double occupancy behavior of hydrogen dimer. The upper plot shows potential energy curves. The lower plot shows the corresponding double occupancies as a function of bond length. 42

Figure 3.3 Potential energy curve and double occupancy behavior of H_6 prism. The upper plot shows potential energy curves. The lower plot shows the corresponding double occupancies as a function of bond length. 43

Figure 3.4 Potential energy curve and double occupancy behavior of H_6 ring. The upper plot shows potential energy curves. The lower plot shows the corresponding double occupancies as a function of bond length. 43

Figure 3.5 Potential energy curve and double occupancy behavior of H_8 ring. The upper plot shows potential energy curves. The lower plot shows the corresponding double occupancies as a function of bond length. 44

Figure 3.6 Potential energy curve and double occupancy behavior of H_8 grid. The upper plot shows potential energy curves. The lower plot shows the corresponding double occupancies as a function of bond length. 44

Figure 3.7 Potential energy curve and double occupancy behavior of H_8 cube. The upper plot shows potential energy curves. The lower plot shows the corresponding double occupancies as a function of bond length. 45

Figure 3.8 Energy curve of H2 calculated by QUAMB-based CMR, as well as QUAMBO-based FCI and large-basis FCI results. The QUAMBOs are constructed from 6-311G(p) basis-set orbitals. 46

Figure 3.9 Potential energy curves of N_2 and F_2. Included are the CMR and FCI results performed on QUAMBOs constructed from aug-cc-pVTZ basis set. Available experimental data [3, 4] are also included. 47

Figure 3.10 Potential energy curves of CO and HF. Included are the CMR and FCI results performed on QUAMBOs constructed from aug-cc-pVTZ basis set. Available experimental data [5] are also included. 48

Figure 3.11 Potential energy curves of NH_3 and CH_4. Included are the CMR and FCI results performed on QUAMBOs constructed from aug-cc-pVTZ basis set. 48

Figure 4.1 Comparison of direct treatment and second variational treatment for spin-orbit effects. The left plot shows the direct treatment including SOC in Dirac equations, which requires setting up and diagonalizing a large matrix. The right plot shows the second variational treatment, in which the SOC is treated as the perturbation only for lowest-lying orbitals. 53

Figure 4.2 Comparison of two methods for the total energy change in terms of λ for FCC crystals Al(top), Pt(middle) and Pu(bottom). Energies from SCC at different λs are indicated as red solid circles, and the solid curves are calculated from CCI. 57

Figure 4.3 Comparison of two methods for magnetic anisotropy energy calculations for FePt and CoPt at different values of λ. Red dots indicate the MAE calculated from self-consistent calculations, while the solid line is the MAE acquired from integration over the coupling constant. 58

Figure 5.1 The self-consistency cycle in DMFT calculations. 64

Figure 5.2 The self-consistency cycle in DFT+DMFT calculations. 65

Figure 5.3 The left panel is the postperovskit structure of CaIrO3 projected on the *bc* plane, and the right one is the projection on the *ab* plane. Ca, Ir, and O atoms are represented by circles with large, medium, and small sizes, respectively. The conventional unit cell is indicated by dash lines. 67

Figure 5.4 Magnetic momentum of Ir atom in $CaIrO_3$ as a function of temperature. Included are total, orbital, and spin magnetic moments. 70

Figure 5.5 Density of states of $CaIrO_3$ at 464K obtained from DFT+DMFT calculations. The upper plot shows the total and partial-d density of states. The lower plot shows the spin-up and spin-down projected density of states for $j_{\text{eff}} = 1/2$ and $j_{\text{eff}} = 3/2$. 71

Figure 5.6 Density of states at 232K obtained from DFT+DMFT calculations. The upper plot shows the total and partial-d density of states. The lower plot shows the spin-up and spin-down projected density of states for $j_{\text{eff}} = 1/2$ and $j_{\text{eff}} = 3/2$. 72

Figure 5.7 Density of states at 203K obtained from DFT+DMFT calculations. The upper plot shows the total and partial-d density of states. The lower plot shows the spin-up and spin-down projected density of states for $j_{\text{eff}} = 1/2$ and $j_{\text{eff}} = 3/2$. 73

Figure 5.8 Density of states at 116K obtained from DFT+DMFT calculations. The upper plot shows the total and partial-d density of states. The lower plot shows the spin-up and spin-down projected density of states for $j_{\text{eff}} = 1/2$ and $j_{\text{eff}} = 3/2$. 74

Figure 5.9 Band structure at 116K, obtained by DFT+DMFT calculations. 75

ACKNOWLEDGEMENTS

First and foremost, I would like to thank my advisor, Dr. Kai-Ming Ho for guiding and supporting me throughout my graduate education. I would also like to thank my group members who made my Ph.D. study a very pleasant experience and collaborators who contributed a lot in my research. Lastly, I would like to thank my parents for encouraging me to finish my Ph.D. program and my lovely wife for all of her support.

This work was supported by the U.S. Department of Energy (DOE), Office of Science, Basic Energy Sciences, Materials Science and Engineering Division, including the computer time support from the National Energy Research Scientific Computing Center (NERSC) in Berkeley, CA. The research was performed at Ames Laboratory, which is operated for the U.S. DOE by Iowa State University under Contract No. DE-AC02-07CH11358.

CHAPTER 1. INTRODUCTION

In 1972, Philip Warren Anderson published in Science a well-known article called "More Is Different" [6], writing

> The behavior of large and complex aggregates of elementary particles, it turns out, is not to be understood in terms of a simple extrapolation of the properties of a few particles.

which suggests that the correlated behavior of many microscopic particles can lead to an unexpected collective phenomena. This is the so-called emergence. In condensed matter physics, the collective properties of electrons are of great importance in understanding many phenomena, such as superconductivity, magnetism, phase transitions, and spin-charge coupling. Despite that theoretical tools like density functional theory (DFT) [7, 8] have successfully explained physical properties of numerous materials, we still have many phenomena hard to understand in strongly correlated electron systems with open d and f shells. These localized orbitals enhance the Coulomb repulsion, and therefore the strongly correlated electrons cannot be described as non-interacting independent ones. Furthermore, the interplay of strong correlation, spin-orbit coupling, crystal field, and spin-charge coupling causes the d and f electron systems to show a collection of exotic phenomena and display a great sensitivity to the external influences, including temperature, doping, pressure, stress, or applied magnetic field. Understanding the underlying principles are great challenges for modern experimental and theoretical physics.

A variety of quantum many-body methods have been developed for studying the strongly correlated electron systems. We have also proposed a computationally efficient

and accurate approach, named the correlation matrix renormalization (CMR) method [9–11], to address the challenges. The initial implementation of the CMR method is designed for molecules which have theoretical advantages, including small size of system, manifest mechanism and strongly correlation effect such as bond breaking process. The theoretic development and benchmark tests of the CMR method are included in this thesis. Meanwhile, ground state total energy is the most important property of electronic calculations. We also investigated an alternative approach to calculate the total energy, and extended this method for magnetic anisotropy energy (MAE) of ferromagnetic materials. In addition, another theoretical tool, dynamical mean-field theory (DMFT) on top of the DFT [12–14] , has also been used in electronic structure calculations for an Iridium oxide to study the phase transition, which results from an interplay of the d electrons' internal degrees of freedom.

The thesis is organized as follows.

Chapter 2 offers a brief introduction to the theoretical background of many-body quantum theory. After introducing the Hamiltonian, we start with the classical Hartree-Fock (HF) approximation, which contains some elementary concepts and is still the cornerstone of many modern quantum techniques. Later we present the basics of DFT, including the theorems of Hohenberg and Kohn [7] as well as the Kohn-Sham equations [8]. After the theoretical background, we discuss the practical aspects of the HF an DFT method, such as the linear-combination-of-atomic-orbitals (LCAO) ansatz [15], single-particle equations, and basis sets. A large fraction is devoted to the basis sets, in that it is a central concept in the computational implementations of many stat-of-the-art quantum methods.

Chapter 3 describes the formalism, methodology, and application of the CMR method. Employing the Gutzwiller wavefunction [16, 17], the CMR method can evaluate the local on-site Hamiltonian accurately, and further approximate the nonlocal one- and two-electron density matrix with renormalization factors. Firstly, we applied the CMR on an

analytically solvable system, the hydrogen dimer with minimal basis set. Through comparison of the exact analytical solution, we proposed two approaches to reduce the errors introduced by the CMR: a modified form of the renormalization factor and a sum-rule term added in the many-body Hamiltonian. Then we performed benchmark calculations on multiple molecules composed of light elements, and further compared the results of CMR with that of full configuration interaction (FCI) method and experiments. Here the CMR calculations were carried out involving the quasi-atomic minimal-basis-set orbitals (QUAMBO), which was developed previously by our group and can recover a large percentage of the electron correlation energy [18, 19].

Chapter 4 addresses an alternative method for MAE calculations, together with the practical analysis of MAE in ferromagnetic materials. After introducing the formalism of coupling constant integration (CCI) method, we report numerical evaluations of the efficiency and accuracy for this approach as an alternative way for total energy calculations. We then compared the CCI method with self-consistent-field calculations (SCC) for energy changes due to spin-orbit effects. The results show that the CCI can reach the accuracy of SCC with only few sampling points, proving the future applicability for perturbation theory. We further illustrate that the MAE, defined as the difference between total energies, can also be calculated through the CCI method with high accuracy in ferromagnetic materials. The CCI also justifies the analysis of MAE in terms of the spin-orbit energy, where we show it can provide useful detailed orbital contribution information.

Chapter 5 explains how we employ the DFT+DMFT method to study the ground state transition in $CaIrO_3$ [20]. We first briefly introduce the DMFT method and its combination with the DFT. Then we performed DFT+DMFT calculations for $CaIrO_3$ at different temperatures to investigate the metal-insulator transition (MIT), which results from the interplay of on-site Coulomb repulsion, spin-orbit coupling, and crystal field. The calculations show that the MIT is accompanied with a magnetic transition,

indicating that the insulating ground state of $CaIrO_3$ should be classified into Slate insulator instead of Mott insulator.

CHAPTER 2. METHODS IN MANY-BODY QUANTUM THEORY

Before reviewing fundamental background of many-body theory, we first state that all equations in this thesis are in form of atomic units, in which the elementary charge e, the rest mass of electron m_e, the reduced Planck constant $\hbar$, and the permittivity of vacuum $4\pi\epsilon_0$ are all defined as unity.

2.1 Many-body Hamiltonian

A molecule or solid can be considered as a collection of nuclei and electrons which are interacting electromagnetically. The many-body hamiltonian for this system is:

$$\begin{aligned}\mathcal{H} = &-\frac{1}{2}\sum_i \frac{\nabla^2_{\mathbf{R}_i}}{M_i} - \frac{1}{2}\sum_i \nabla^2_{\mathbf{r}_i} - \sum_{i,j}\frac{Z_i}{|\mathbf{R}_i - \mathbf{r}_j|} \\ &+ \frac{1}{2}\sum_{i\neq j}\frac{1}{|\mathbf{r}_i - \mathbf{r}_j|} + \frac{1}{2}\sum_{i\neq j}\frac{Z_i Z_j}{|\mathbf{R}_i - \mathbf{R}_j|}.\end{aligned} \tag{2.1}$$

The nucleus with mass M_i is located at $\mathbf{R}_i$, while the electron is at $\mathbf{r}_i$. The first term is kinetic energy operator for nuclei, the second term for electrons. The last three terms are electron-nucleus Coulomb interactions, electron-electron interactions, nucleus-nucleus interactions respectively. It can be seen that each particle is coupled with all other particles. The scale of number of particles in large molecules and bulk solid is far beyond the capability of supercomputers today. To solve this many-body problem, it is inevitable to introduce approximations. The Born-Oppenheimer approximation keeps the nuclei fixed, and assumes electrons to be in equilibrium instantaneously due to the external

field from interactions of nuclei. Now the kinetic energy operator of nuclei disappears, and nucleus-nucleus interaction becomes a constant term. The problem is reduced to a many-electron problem, which can be written as the sum of electronic kinetic term, electron-electron term and external field term:

$$\begin{aligned}\mathcal{H} =& \mathcal{T} + \mathcal{V} + \mathcal{V}_{ext} \\ =& -\frac{1}{2}\sum_i \nabla^2_{\mathbf{r}_i} + \frac{1}{2}\sum_{i\neq j}\frac{1}{|\mathbf{r}_i - \mathbf{r}_j|} - \sum_{i,j}\frac{Z_i e^2}{|\mathbf{R}_i - \mathbf{r}_j|}.\end{aligned} \tag{2.2}$$

Since we have the many-body Hamiltonian, the variational principle provides a direct way to determine the ground-state wavefunction Ψ and total energy E_0, expressed as,

$$\begin{aligned}E_0 &= \min_{\Psi} E[\Psi] \\ &= \min_{\Psi} \langle \Psi | \mathcal{T} + \mathcal{V} + \mathcal{V}_{ext} | \Psi \rangle.\end{aligned} \tag{2.3}$$

However, it is impossible to search over all eligible N-electron wavefunctions $\{\Psi\}$, so further approximations are still needed.

2.2 Hartree-Fock approximation

The Hartree-Fock (HF) approximation searches the ground-state wavefunction not through all eligible wavefunctions but only from a small subset which includes all anti-symmetrized products (Slater determinants) of spin orbitals. The HF approximation is of conceptual importance, and also a cornerstone of wavefunction-based quantum chemical methods. In HF scheme, the N-electron wavefunction is approximated by an antisymmetrized product of N one-electron spin orbitals, referred as Slater determinants Ψ_{HF}:

$$\begin{aligned}\Psi_{\mathrm{HF}} &= \frac{1}{\sqrt{N!}}\det\{\psi_{\nu_1}(\mathbf{r}_1)\psi_{\nu_2}(\mathbf{r}_2)\ldots\psi_{\nu_N}(\mathbf{r}_N)\} \\ &= \frac{1}{\sqrt{N!}}\begin{vmatrix} \psi_{\nu_1}(\mathbf{r}_1) & \psi_{\nu_1}(\mathbf{r}_2) & \ldots & \psi_{\nu_1}(\mathbf{r}_N) \\ \psi_{\nu_2}(\mathbf{r}_1) & \psi_{\nu_2}(\mathbf{r}_2) & \ldots & \psi_{\nu_2}(\mathbf{r}_N) \\ \vdots & \vdots & \ddots & \vdots \\ \psi_{\nu_N}(\mathbf{r}_1) & \psi_{\nu_N}(\mathbf{r}_2) & \ldots & \psi_{\nu_N}(\mathbf{r}_N) \end{vmatrix}.\end{aligned} \tag{2.4}$$

The only flexibility in the Slater determinants is the variation of spin orbitals $\{\psi_i\}$. The "best" Slater determinant minimizes the expectation of Hamiltonian. The HF energy has the form of [21],

$$\begin{aligned}E_{\mathrm{HF}} &= \langle\Psi_{\mathrm{HF}}|\mathcal{H}|\Psi_{\mathrm{HF}}\rangle \\ &= T_{\mathrm{HF}} + V_H + V_x \\ &= \sum_{i=1}^{N} t_{ii} + \frac{1}{2}\sum_{i,j}^{N} u(ii;jj) - \frac{1}{2}\sum_{i,j}^{N} u(ij;ji)\end{aligned} \tag{2.5}$$

where

$$t_{ii} = \int \psi_i^*(\mathbf{r})\left\{-\frac{1}{2}\nabla^2 - \sum_j \frac{Z_j e^2}{|\mathbf{R}_j - \mathbf{r}|}\right\}\psi_i(\mathbf{r})\,d\mathbf{r} \tag{2.6}$$

defines the contribution due to kinetic energy of on-site electrons and Coulomb interaction between nucleus and electron,

$$u(ii;jj) = \int\int |\psi_i(\mathbf{r}_1)|^2 \frac{1}{|\mathbf{r}_1 - \mathbf{r}_2|}|\psi_j(\mathbf{r}_2)|^2\,d\mathbf{r}_1 d\mathbf{r}_2 \tag{2.7}$$

is the Coulomb integral, and

$$u(ij;ji) = \int\int \psi_i^*(\mathbf{r}_1)\psi_j^*(\mathbf{r}_2)\frac{1}{|\mathbf{r}_1 - \mathbf{r}_2|}\psi_j(\mathbf{r}_1)\psi_i(\mathbf{r}_2)\,d\mathbf{r}_1 d\mathbf{r}_2 \tag{2.8}$$

is the exchange integral. We utilize the Slater determinant as approximation to the true N-electron wavefunction. In the other way, the Slater determinant can be considered as an exact wavefunction of a system consisting of N non-interacting electrons. In Eq. 2.5, the first term T_{HF} is then regarded as the kinetic energy of the non-interacting N-electron

system, the second term V_H stands for the Hartree contribution, and the third one V_x stands for the exchange contribution.

In order to minimize the HF energy, we need introduce Lagrangian multipliers to satisfy the orthonormal conditions of spin orbitals, and then the HF equations can be derived [21] as,

$$\hat{f}\psi_i(\mathbf{r}) = \varepsilon_i \psi_i(\mathbf{r}). \tag{2.9}$$

The Lagrangian multipliers ε_i have the physical meaning of orbital energies, and $\hat{f}$ is the so-called Fock operator defined as,

$$\hat{f}_i = -\frac{\hbar^2}{2m_e}\nabla^2 - \frac{1}{4\pi\epsilon_0}\sum_j \frac{Z_j e^2}{|\mathbf{R}_j - \mathbf{r}|} + \sum_j \left[\hat{J}_j(\mathbf{r}) - \hat{K}_j(\mathbf{r})\right] \tag{2.10}$$

where

$$\hat{J}_j(\mathbf{r}) = \int |\psi_j(\mathbf{r}')|^2 \tfrac{1}{|\mathbf{r}-\mathbf{r}'|}\, d\mathbf{r}' \tag{2.11}$$

$$\hat{K}_j(\mathbf{r})\psi_i(\mathbf{r}) = \int \psi_j(\mathbf{r}') \tfrac{1}{|\mathbf{r}-\mathbf{r}'|} \psi_i(\mathbf{r}')\, d\mathbf{r}' \psi_j(\mathbf{r}). \tag{2.12}$$

2.3 Density functional theory

In 1964, the framework of DFT was formally established by Hohenberg and Kohn [7]. The fundamental theorem in DFT states that, all observable quantities for the ground-state of a many-electron system with an external potential can be determined uniquely by the ground state electron density. The ground-state total energy for the many-body Hamiltonian $\mathcal{H}$ can be written as a functional of the ground-state electron density:

$$\begin{aligned} E[\rho] =& \langle \Psi | \mathcal{T} + \mathcal{V} | \Psi \rangle + \langle \Psi | \mathcal{V}_{ext} | \Psi \rangle \\ =& F[\rho] + \int \rho(\mathbf{r}) V_{ext}(\mathbf{r}) d\mathbf{r}. \end{aligned} \tag{2.13}$$

The density operator $\hat{\rho}$ is defined as $\hat{\rho}(\mathbf{r}) = \sum_{i=1}^{N} \delta(\mathbf{r}_i - \mathbf{r})$, and its evaluation has the form of,

$$\begin{aligned}\rho(\mathbf{r}) =& \langle \Psi | \hat{\rho} | \Psi \rangle \\ =& \sum_{i=1}^{N} \int \Psi^*(\mathbf{r}_1, \cdots, \mathbf{r}_N) \delta(\mathbf{r}_i - \mathbf{r}) \Psi(\mathbf{r}_1, \cdots, \mathbf{r}_N)\, d\mathbf{r}_1 \cdots d\mathbf{r}_N.\end{aligned} \tag{2.14}$$

The theorem also states that, the total energy $E[\rho]$ reaches the minimal value for the ground-state density. In other words, we can minimize the energy functional in order to find the correct ground state density.

The Hohenberg-Kohn theorems states the unique mapping between the density and the ground-state energy, but no guidance at how the functional can be constructed. To tackle the problem, Kohn and Sham proposed an approach in 1965 [8], which puts the density functional theorems into practice.

The functional $F[\rho]$ in Eq. 2.13 contains the kinetic energy, the classical Coulomb interaction and non-classical part. The non-classical portion includes the exchange interaction, the self-interaction correction, and electron correlation effects. $F[\rho]$ has the form of

$$F[\rho] = T[\rho] + V_H[\rho] + E_{\text{ncl}}[\rho]. \tag{2.15}$$

Here the classical electrostatic energy functional $V_H[\rho]$ is written as,

$$V_H[\rho] = \frac{1}{2} \int \int \frac{\rho(\mathbf{r})\rho(\mathbf{r}')}{|\mathbf{r} - \mathbf{r}'|}\, d\mathbf{r} d\mathbf{r}' \tag{2.16}$$

The kinetic energy can be approximated from a non-interacting reference system, and the remainder is merged to the non-classical electron-electron interaction:

$$\begin{aligned}F[\rho] &= T[\rho] + V_H[\rho] + E_{\text{ncl}}[\rho] \\ &= \underbrace{T_{\text{HF}}[\rho] + V_c[\rho]}_{T[\rho]} + V_H[\rho] + E_{\text{ncl}}[\rho] \\ &= T_{\text{HF}}[\rho] + V_H[\rho] + \underbrace{E_{\text{ncl}}[\rho] + V_c[\rho]}_{E_{xc}[\rho]}.\end{aligned} \tag{2.17}$$

Here $E_{xc}[\rho]$ is the so-called exchange-correlation energy functional, which contains everything that is unknown.

Suppose that nucleus-electron attraction is the only external field, the total energy functional can then be written as,

$$\begin{aligned} E[\rho] =& T_{\mathrm{HF}}[\rho] + V_H[\rho] + E_{xc}[\rho] + E_{N-e}[\rho] \\ =& -\frac{1}{2}\sum_i^N \langle\psi_i|\nabla^2|\psi_i\rangle + \frac{1}{2}\sum_{i,j}^N \int\int |\psi_i(\mathbf{r})|^2 \frac{1}{|\mathbf{r}-\mathbf{r}'|}|\psi_j(\mathbf{r})\, d\mathbf{r}d\mathbf{r}' \\ &+ E_{xc}[\rho] - \sum_{i,j}\int \frac{Z_i}{|\mathbf{R}_i - \mathbf{r}|}|\psi_j(\mathbf{r})|^2\, d\mathbf{r}. \end{aligned} \tag{2.18}$$

Many approximations to the form of $E_{xc}[\rho]$ have been proposed, like the local density approximation (LDA), the local spin-density approximation (LSDA), and the generalized gradient approximation (GGA).

Similar to the HF equations, the variational principle gives the famous Kohn-Sham (KS) equations:

$$\hat{H}_{KS}\psi_i(\mathbf{r}) = \epsilon_i\psi_i(\mathbf{r}) \tag{2.19}$$

where

$$\hat{H}_{KS} = -\frac{1}{2}\nabla_i^2 + \int \frac{\rho(\mathbf{r}')}{|\mathbf{r}-\mathbf{r}'|}\, d\mathbf{r}' + \hat{V}_{xc} + \hat{V}_{ext}. \tag{2.20}$$

Here the exchange-correlation potential is defined by,

$$\hat{V}_{xc} = \frac{\delta E_{xc}[\rho]}{\delta\rho}. \tag{2.21}$$

One point to mention is that the single-particle wave functions $\{\psi_i\}$ are not physical orbitals of electrons. Similarly, the eigenvalues ϵ_i are also not single-electron energies. Only the total density has a direct physical meaning and it is equal to the electron density of our real target system,

$$\rho(\mathbf{r}) = \sum_i^N |\psi_i(\mathbf{r})|^2. \tag{2.22}$$

2.4 Basic machinery for solving self-consistent equations

A self-consistency problem

Either HF or DFT approximation ends up with a similar set of one-electron equations:

$$\hat{H}_{sp}\psi_i(\mathbf{r}) = \epsilon_i\psi_i(\mathbf{r}). \tag{2.23}$$

Here the $\hat{H}_{sp}$ is called the single-particle Hamiltonian. For HF, the $\hat{H}_{sp}$ depends on the one-electron spin orbitals $\psi_i(\mathbf{r})$. For DFT, the $\hat{H}_{sp}$ is a functional of density $\rho(\mathbf{r})$, which in turn depends on the quasi-particle orbitals $\psi_i(\mathbf{r})$. This means that it is a self-consistency problem: the equations depend on the solutions. A general procedure to solve this paradox is to make use of the iterative approach. Initially, a guessed solution is used to construct the $\hat{H}_{sp}$, and the equation results in a new solution. If the input and output solutions are different, then the output solution can construct a new $\hat{H}_{sp}$, etc. Finally, this series of solutions will converge to a final one that is the target solution. A flow chart is shown to solve the KS equations in Fig. 2.1.

LCAO ansatz

To solve Eq. 2.23 in practice, people make use of the linear-combination-of-atomic-orbitals (LCAO) ansatz, which is introduced by Roothaan in 1951 [15]. In the LCAO scheme, the $\psi_i(\mathbf{r})$ orbitals are expanded by a set of L predefined basis functions $\{\phi_\nu\}$:

$$\psi_i = \sum_{\nu=1}^{L} \phi_\nu c_{\nu i}. \tag{2.24}$$

A complete basis set requires the number L to be infinite, and then every function ψ_i can be exactly expressed by $\{\phi_\nu\}$. In real situation, however, one works with a finite set of basis functions, so it is of importance that such limited set of basis can provide approximation of the exact orbitals ψ_i as accurate as possible. Historically, the basis

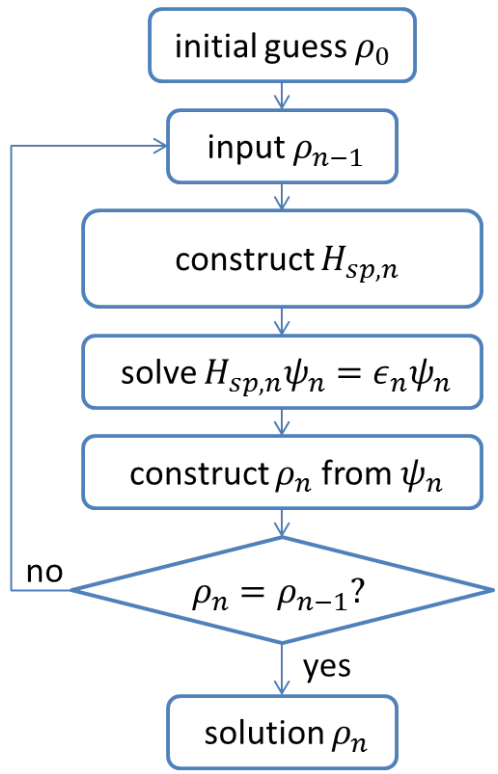

Figure 2.1: Flow chart of self-consistent procedure in solving KS equations.

set was inspired by atomic orbitals for the hydrogen atom, and that is where the name LCAO came from.

The LCAO scheme helps simplify the originally non-linear optimization problem into a linear one. Given a basis set with size L, the Eq. 2.23 becomes,

$$\hat{H}_{sp}\sum_{\nu=1}^{L}|\phi_\nu\rangle c_{\nu i} = \epsilon_i \sum_{\nu=1}^{L}|\phi_\nu\rangle c_{\nu i}. \tag{2.25}$$

Left multiplied $\langle\psi_\mu|$, the equation is given by,

$$\sum_{\nu=1}^{L}\langle\psi_\mu|\hat{H}_{sp}|\phi_\nu\rangle c_{\nu i} = \epsilon_i \sum_{\nu=1}^{L}\langle\psi_\mu|\phi_\nu\rangle c_{\nu i}. \tag{2.26}$$

It leads to a matrix form:

$$\begin{bmatrix} \cdots & \cdots & \cdots \\ \vdots & H_{\mu\nu} - \epsilon_i S_{\mu\nu} & \vdots \\ \cdots & \cdots & \cdots \end{bmatrix} \begin{bmatrix} c_{1i} \\ c_{2i} \\ \vdots \\ c_{Li} \end{bmatrix} = \begin{bmatrix} 0 \\ 0 \\ \vdots \\ 0 \end{bmatrix} \tag{2.27}$$

where the matrix element of single-particle Hamiltonian in such basis set is $H_{\mu\nu} = \langle\psi_\mu|\hat{H}_{sp}|\phi_\nu\rangle$ and the matrix element of overlap matrix is

$$S_{\mu\nu} = \langle\psi_\mu|\phi_\nu\rangle. \tag{2.28}$$

Eq. 2.27 is a typical secular equation of matrix $\{H_{\mu\nu}\}$. Diagonalization of $\{H_{\mu\nu}\}$ will lead to L eigenvectors and eigenvalues, which correspond to the set of expansion coefficients $\{c_{\nu i}\}$ and Lagrangian multipliers ϵ_i, $i = 1, 2, \cdots, L$.

The electron density in Eq. 2.22 can now be computed by:

$$\begin{aligned}\rho(\mathbf{r}) &= \sum_i^N |\psi_i(\mathbf{r})|^2 \\ &= \sum_i^N \sum_{\mu,\nu}^L c^*_{\mu i} c_{\nu i} \phi^*_\mu(\mathbf{r})\phi_\nu(\mathbf{r}).\end{aligned} \tag{2.29}$$

From the expression of ρ, it can be seen that the expansion coefficients also contain all information about the electron density, which is usually expressed by a density matrix P defined as:

$$P_{\mu\nu} = \sum_i^N c^*_{\mu i} c_{\nu i} \tag{2.30}$$

2.5 Basis sets in molecular systems

As mentioned previously, the basis functions are in practice finite, and the choice in the past could be atomic orbitals of the hydrogen atom. Nowadays, a collection of basis functions have been generated according to different criteria, and some of them do not resemble atomic orbitals anymore. In the following, some typical types of basis sets, which are widely used in quantum chemistry calculations, are introduced briefly.

The Gaussian-type-orbitals (GTO) is has the general form of:

$$\phi^{GTO} = N x^l y^m z^n e^{-\alpha r^2} \tag{2.31}$$

where N is the normalization factor ensuring that $\langle\phi_\mu|\phi_\nu\rangle = \delta_{\mu\nu}$. The sum of l, m, n, denoted as L, is used to classify the GTO as s-functions ($L = 0$), p-functions ($L = 1$),

and so on. One may find that the number of GTO functions exceeds $(2l+1)$ for $L > 1$. For example, when $L = 2$, it contains six basis functions, but one of them is not d-type but an s-type.

The Slater-type-orbitals (STO) seems more natural from the physical point of view, which has the form:

$$\phi^{STO} = N r^{n-1} e^{-\alpha r} Y_{lm}(\theta, \varphi). \tag{2.32}$$

However, two-electron integrals for these STO functions are very time consuming, whereas efficient algorithms exist for GTOs since analytical integrations are available.

The contracted Gaussian function (CGF) is designed to resemble a single STO function from GTO functions. It can be expressed as,

$$\phi^{CGF} = \sum_a c_a \phi_a^{GTO}. \tag{2.33}$$

One general category of basis sets is the minimal basis set. It is a collection of CGF sets, in which one CGF is utilized for each atomic orbital up to the valence orbitals. For example, in STO-3G basis set [22], three primitive GTO functions comprise one CGF, and one hydrogen atom has only one CGF function.

Another category of basis sets is the extended basis set. Clearly, minimal basis set is not sophisticated for quantitative calculations in real world. The double-zeta functions are therefore introduced, in which a linear combination of two CGFs is utilized for one atomic orbital. The triple- and quadruple-zeta basis sets perform the same way, except the set of CGFs is tripled or quadrupled. However, it takes too much effort to apply double-zeta for every atomic orbital, so in split-valence method, the doubled set of functions is limited only to the valence orbitals. For example, one core-orbital CGF in 3-21G basis set [23] is formed by three GTO functions, and one valence orbital is comprised by two CGFs, one with two GTO and the other with one GTO:

$$\begin{aligned} \phi &= c_1 \phi_1^{CGF} + c_2 \phi_2^{CGF} \\ &= c_1 (\phi_1^{GTO} + \phi_2^{GTO}) + c_2 \phi_3^{GTO} \end{aligned} \tag{2.34}$$

In some applications, the extended basis set is also augmented with polarization functions, that is, functions of higher angular momentum than occupied atomic orbitals in these atoms. The purpose is to consider the distortion of atomic orbitals when atoms are brought together. Typical examples are the 6-31G(d) and 6-31G(d,p) basis sets developed by George Petersson and coworkers [24].

Modern examples of basis sets usually contain triple-, quadruple-, or even quintuple-zeta basis sets augmented by polarization functions with higher angular momentum, like the cc-pVDZ, cc-pVTZ, and cc-pVQZ, also named as Dunning's correlation consistent basis sets [25].

2.6 Basis sets in periodic materials

With the advances in computing capability during last decades, the density functional theory has proved to be a computationally tractable tool in materials science. Practitioners at that time are divided into two communities: one using pseudopotentials with simple plane waves basis sets and the other using all-electron methods with basis sets like the linearized muffin-tin orbital (LMTO) and linearized augmented plane wave (LAPW).

2.6.1 Plane waves and pseudopotential

In periodic materials, plane wave functions serves as the basis set, generally written as,

$$\phi^{PW} = e^{i\mathbf{k}\cdot\mathbf{r}}. \tag{2.35}$$

Here the momentum $\mathbf{k}$ is a good quantum number of periodic Hamiltonian. According to Bloch's theorem, any eigenfunction $\psi_{\mathbf{k}}$ of a crystal lattice with reciprocal lattice vectors $\mathbf{G}$ has the form of $\psi_{\mathbf{k}}(\mathbf{r}) = e^{i\mathbf{k}\cdot\mathbf{r}} \sum_{\mathbf{G}} c^{\mathbf{k}}_{\mathbf{G}} e^{i\mathbf{G}\cdot\mathbf{r}}$. The basis function for $\psi_{\mathbf{k}}(\mathbf{r})$ is therefore:

$$\phi_{\mathbf{k},\mathbf{G}} = e^{i(\mathbf{k}+\mathbf{G})\cdot\mathbf{r}}. \tag{2.36}$$

It can be seen that this set of basis functions is **k**-dependent. The size of basis set should also be finite for practical reason, and it can be done by limiting momentum with $(\mathbf{k}+\mathbf{G}) \leq K_{max}$. The corresponding free electron energy is the so-called cut-off energy: $E_{\text{cut}} = K_{max}^2/2$. Given the momentum **k** and L basis functions $\{\phi_{\mathbf{k},\mathbf{G}}\}$, the eigenfunction problem will provide actually L sets of eigenvalues $\epsilon_{\mathbf{k},n}$ and eigenvectors $\psi_{k,n}$, where n is the index for eigenvectors within the same momentum and is usually called the band index. Therefore, each eigenfunction is labeled uniquely by n and **k**.

However, it requires a huge number of plan wave basis to describe the oscillating portion of the wave function in the region close to the nucleus, while it is the outer regions where chemistry happens. Therefore an approximation is proposed to replace the strong core potential with a pseudopotential that yields smooth wavefunctions inside the atom. The pseudopotential wave functions can then be well represented by plane waves with low cut-off energy.

2.6.2 LAPW methods

LAPW basis set is one typical member of a family of basis sets that treats the inner and interstitial regions differently. The fundamental one is the augmented plane wave (APW) basis set, and LAPW is a modification of it.

The idea of the APW method [26–28] is to divide the space into two regions shown in Fig. 2.2, and to use different basis functions for these regions. The region close to the nucleus is called muffin-tin region (denoted as S), in which wavefunction is described by atomic like functions. In the interstitial region (denoted as I) between atoms, the potential is smoother and wavefunction is expanded by plane waves.

Hence, one APW basis $\phi_{\mathbf{k},\mathbf{G}}(\mathbf{r})$ at a particular k-point can then be divided into two parts. In the interstitial region I, the basis has the form of plane wave:

$$\phi_{\mathbf{k},\mathbf{G}}(\mathbf{r}) = \Omega^{-1/2} e^{i(\mathbf{k}+\mathbf{G})\cdot\mathbf{r}}, \qquad \mathbf{r} \in I. \tag{2.37}$$

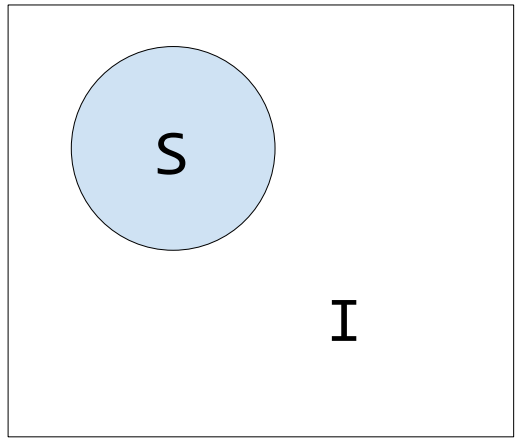

Figure 2.2: Sketch of muffin-tin (S) and interstitial (I) regions in a unit cell.

Here, Ω is the cell volume. In the muffin-tin region S_α for atom α, the basis $\phi_{\mathbf{k},\mathbf{G}}(\mathbf{r})$ is expanded with spherical harmonics Y_{lm}:

$$\phi^{\alpha}_{\mathbf{k},\mathbf{G}}(\mathbf{r}) = \sum_{lm} A^{\alpha,\mathbf{k}+\mathbf{G}}_{lm} u^{\alpha}_{l}(\mathbf{r}', E) Y_{lm}(\mathbf{r}'), \qquad \mathbf{r} \in S_\alpha. \tag{2.38}$$

Here, $\mathbf{r}'$ defines the distance with respect to the center $\mathbf{r}_\alpha$ of the muffin-tin sphere, given by $\mathbf{r}' = \mathbf{r} - \mathbf{r}_\alpha$. u^{α}_{l} is the regular solution of the radial Schrödinger equation for atom α:

$$\left[-\frac{d^2}{2dr^2} + \frac{l(l+1)}{2r^2} + V(r) - E \right] r u_l(r) = 0. \tag{2.39}$$

The E is yet undetermined parameter. The expansion coefficient $A^{\alpha,\mathbf{k}+\mathbf{G}}_{lm}$ is actually known according to the requirement of continuity on the sphere boundaries where $\mathbf{r}' = \mathbf{R}_\alpha$, given by [28],

$$A^{\alpha,\mathbf{k}+\mathbf{G}}_{lm} = \frac{4\pi i^l}{\sqrt{\Omega} u^{\alpha}_{l}(\mathbf{R}_\alpha)} j_l(|\mathbf{k}+\mathbf{G}|\mathbf{R}_\alpha) Y^*_{lm}(\mathbf{k}+\mathbf{G}). \tag{2.40}$$

where $j_l(\cdot)$ is the Bessel function of order l. The set of spherical harmonics is supposed to be infinite, but in practice it is truncated at a maximal limit $l_{\max}$ for the summation in Eq. 2.38. To sum up, one APW basis can be written like a piecewise function [28]:

$$\phi_{\mathbf{k},\mathbf{G}}(\mathbf{r}) = \begin{cases} \Omega^{-1/2} e^{i(\mathbf{k}+\mathbf{G})\cdot\mathbf{r}} & \mathbf{r} \in I \\ \sum_{lm} A^{\alpha,\mathbf{k}+\mathbf{G}}_{lm} u^{\alpha}_{l}(\mathbf{r}', E) Y_{lm}(\mathbf{r}') & \mathbf{r} \in S_\alpha. \end{cases} \tag{2.41}$$

Then, an eigenfunction expanded by such APW basis is the same as the plane wave expansion, written as,

$$\psi_{\mathbf{k},n} = \sum_{\mathbf{G}} c_{\mathbf{G}}^{\mathbf{k}} \phi_{\mathbf{k},\mathbf{G}}. \tag{2.42}$$

However, the parameter E is unknown yet. At the beginning, a guessed E is required to construct the basis set as well as the Hamiltonian. The diagonalization will give a series of eigenvalues, and E is supposed to be one of them. If it is not true, a second trial is needed. The procedure is repeated for every band energies at a particular k-point, which causes the APW method much slower than pseudopotential.

The LAPW method makes it possible to calculate the radial function $u_l^\alpha(\mathbf{r}')$ from some energy E_0 instead of the exact band energy. According to the Taylor expansion of

$$u_l^\alpha(\mathbf{r}', \epsilon) \approx u_l^\alpha(\mathbf{r}', E_0) + (\epsilon - E_0)\dot{u}_l^\alpha(\mathbf{r}', E_0) + O((\epsilon - E_0)^2), \tag{2.43}$$

the basis can then be defined as [28],

$$\phi_{\mathbf{k},\mathbf{G}}(\mathbf{r}) = \begin{cases} \Omega^{-1/2} e^{i(\mathbf{k}+\mathbf{G})\cdot\mathbf{r}} & \mathbf{r} \in I \\ \sum_{lm} \left[A_{lm}^{\alpha,\mathbf{k}+\mathbf{G}} u_l^\alpha(\mathbf{r}', E_l) + B_{lm}^{\alpha,\mathbf{k}+\mathbf{G}} \dot{u}_l^\alpha(\mathbf{r}', E_l) \right] Y_{lm}(\mathbf{r}') & \mathbf{r} \in S_\alpha. \end{cases} \tag{2.44}$$

where the function forms of $A_{lm}^{\alpha,\mathbf{k}+\mathbf{G}}$ and $B_{lm}^{\alpha,\mathbf{k}+\mathbf{G}}$ need satisfy the continuous boundary conditions in both zero order and first order (slope). Here u_l^α with different angular momentums do not use a universal energy, but E_l for every l. The reason is that the LAPW method does not need exact band energy like APW to form the wavefunction. The choice of E_0 of Eq. 2.43 has a relatively large range, so that multiple bands can be treated together with a single set of E_l. This procedure makes it possible to yield energy bands at a given k-point with only one single diagonalization [28].

CHAPTER 3. CORRELATION MATRIX RENORMALIZATION THEORY

3.1 Introduction

One of the major challenges in condensed matter physics is to develop an efficient *ab initio* method that can provide accurate descriptions even for strongly correlated electron systems. Multiple classes of methods are widely used: density functional theory (DFT), quantum-chemistry method, quantum Monte Carlo method and hybrid approaches.

The Kohn-Sham density functional theory (KS-DFT) [7, 8], has been the dominant computational tool in calculations for physical properties of many materials, but current available approximations for KS-DFT fail at describing the strongly electron correlation effects. However, the computational cost is relatively lower than traditional quantum-chemistry methods, such as the Hartree-Fock (HF) theory.

Wavefunction-based quantum-chemical methods can provide very accurate description, and the computational cost has also been greatly reduced recently, e.g., by using density-matrix renormalization group [29–31]. However, due to the computational complexity, the application is still limited to finite systems.

In recent years, the quantum Monte Carlo (QMC) method has emerged as a tool to provide reference many-electron energies for a variety of solid materials. It has also improved recently, and some studies have been reported for realistic correlated materials [32–34]. Nevertheless, this method, like advanced quantum chemical calculations, still has heavy computational load, which restricts the system sizes that can be studied.

In the same time, hybrid approaches, which combine traditional DFT with many-body techniques, are highly successful for realistic correlated materials. These approaches include DFT+dynamical mean-field theory (DFT+DMFT) [12–14], DFT+onsite Coulomb interaction (DFT+U) [35, 36], and DFT+Gutzwiller approximation (DFT+GA) [37–42]. Nevertheless, the on-site Coulomb repulsion and the exchange energies are treated as adjustable parameters, so these methods are considered as a semiphenomenological approach. Moreover, the so-called double-counting term is used to subtract the local onsite correlation contributions in DFT, but this term is not well understood theoretically and the choice of it remains open [43–47].

In the last few years, we have developed a computationally efficient and accurate approach, the correlation matrix renormalization (CMR) method, to address the problems [9–11]. This method aims for the ground state total energy calculations for strongly correlated electron systems. We adopt Gutzwiller type variational wavefunctions to calculate the expectation value of many-electron Hamiltonian directly. One of the advantages of this method is the aversion to screened Coulomb parameters and so it is free of double-counting issues. Another advantage is the relative lower computational cost, which scales as N^4 with respect to the system size N, comparable to Hartree-Fock method. We firstly performed benchmark results on a series of molecules, and the calculations for solid materials are under process. When calculating the molecules, we found errors originating from approximations in our CMR method. At first, we introduced a fitted functional of the one-electron renormalization factor to minimize the errors [10]. The disadvantage of this approach is that we need exact results for each element in the reference systems. Later, we proposed a way involving sum-rule corrections to achieve similar accuracy without the fitting procedure [11].

In this chapter, we first briefly review the second quantization for many-particle systems. The second quantization provides a way to formulate quantum theory in terms of occupation numbers of single-particle states, which is used in the formalism of our CMR

method. Next, we discuss the approximations to density matrix, sum rule corrections to minimize the error, and iterative procedure for CMR calculations. Lastly, benchmark results for a series of molecules are presented.

3.2 Second quantization

3.2.1 First quantization

In many-body quantum theory, the system often contains N identical particles, say, electrons. A fundamental assumption for N-particle systems is that particles characterized by the same quantum numbers, namely identical particles, are in principle indistinguishable. If two coordinates are interchanged, the state function can differ from the original one by $+1$ or -1. The corresponding two type of particles are so-called bosons and fermions. For fermions, the indistinguishability leads to the Pauli exclusion principle, that is, two electrons cannot occupy the same state. Another assumption is that any state function for N-particle system can be expressed as a linear combination of products by single-particle basis states. Using the Pauli principle, the N-particle state function for fermions can be built from complete orthonormal single-particle basis $\{\psi_\nu(\mathbf{r})\}$ with expansion coefficients $A_{\nu_1,\ldots,\nu_N}$, written as,

$$\psi(\mathbf{r}_1, \mathbf{r}_2, \ldots, \mathbf{r}_N) = \sum_{\nu_1,\ldots,\nu_N} A_{\nu_1,\ldots,\nu_N} |\psi_{\nu_1}(\mathbf{r}_1)\psi_{\nu_2}(\mathbf{r}_2)\ldots\psi_{\nu_N}(\mathbf{r}_N)| \tag{3.1}$$

where $|\psi_{\nu_1}(\mathbf{r}_1)\psi_{\nu_2}(\mathbf{r}_2)\ldots\psi_{\nu_N}(\mathbf{r}_N)|$ is denoted as Slater determinants:

$$|\psi_{\nu_1}(\mathbf{r}_1)\psi_{\nu_2}(\mathbf{r}_2)\ldots\psi_{\nu_N}(\mathbf{r}_N)| = \begin{vmatrix} \psi_{\nu_1}(\mathbf{r}_1) & \psi_{\nu_1}(\mathbf{r}_2) & \ldots & \psi_{\nu_1}(\mathbf{r}_N) \\ \psi_{\nu_2}(\mathbf{r}_1) & \psi_{\nu_2}(\mathbf{r}_2) & \ldots & \psi_{\nu_2}(\mathbf{r}_N) \\ \vdots & \vdots & \ddots & \vdots \\ \psi_{\nu_N}(\mathbf{r}_1) & \psi_{\nu_N}(\mathbf{r}_2) & \ldots & \psi_{\nu_N}(\mathbf{r}_N) \end{vmatrix}. \tag{3.2}$$

A local one-particle operator $T_i = T(\mathbf{r}_i, \nabla_{\mathbf{r}_i})$ defined on single-particle states described by $\mathbf{r}_i$ can be written as,

$$T_i = \sum_{\nu_a,\nu_b} T_{\nu_b\nu_a} |\psi_{\nu_b}(\mathbf{r}_i)\rangle\langle\psi_{\nu_a}(\mathbf{r}_i)| \tag{3.3}$$

where

$$T_{\nu_b\nu_a} = \int d\mathbf{r}_i\, \psi^*_{\nu_b}(\mathbf{r}_i) T(\mathbf{r}_i, \nabla_{\mathbf{r}_i}) \psi_{\nu_a}(\mathbf{r}_i) \tag{3.4}$$

The corresponding operator in N-particle system is therefore

$$T_{\text{tot}} = \sum_i^N T_i \tag{3.5}$$

Two-particle operators V_{jk}, such as the Coulomb repulsion $\frac{e^2}{4\pi\epsilon_0}\frac{1}{|\mathbf{r}_j - \mathbf{r}_k|}$, can be written as,

$$V_{jk} = \sum_{\substack{\nu_a,\nu_b \\ \nu_c,\nu_d}} V_{\nu_a\nu_b;\nu_c\nu_d} |\psi_{\nu_a}(\mathbf{r}_j)\rangle|\psi_{\nu_c}(\mathbf{r}_k)\rangle\langle\psi_{\nu_d}(\mathbf{r}_k)|\langle\psi_{\nu_b}(\mathbf{r}_j)| \tag{3.6}$$

where

$$V_{\nu_a\nu_b;\nu_c\nu_d} = \int d\mathbf{r}_j d\mathbf{r}_k\, \psi^*_{\nu_a}(\mathbf{r}_j)\psi^*_{\nu_c}(\mathbf{r}_k) V(\mathbf{r}_j - \mathbf{r}_k)\psi_{\nu_d}(\mathbf{r}_k)\psi_{\nu_b}(\mathbf{r}_j). \tag{3.7}$$

Then the operator of the total interaction is usually written as two forms of summation,

$$V_{\text{tot}} = \sum_{j>k}^N V_{jk} = \frac{1}{2}\sum_{j,k\neq j}^N V_{jk}. \tag{3.8}$$

3.2.2 Basic concepts of second quantization

The second quantization representation formulates the many-body quantum theory in terms of occupation numbers of single-particle states. This space is denoted as the Fock space $\mathcal{F}$. The N-particle basis state is built from single-particle basis $\{|\nu\rangle\}$, written as

$$|n_{\nu_1} n_{\nu_2} \cdots\rangle, \tag{3.9}$$

and the summation of occupation numbers must be the total number of particles, that is,

$$\sum_j n_{\nu_j} = N. \tag{3.10}$$

For electrons, $n_{\nu_j} = 0$ or 1. In terms of creation and annihilation operators, denoted $c^\dagger_{\nu_j}$ and c_{ν_j} respectively, the single Slate determinant $|\psi_{\nu_{n_1}}(\mathbf{r}_1)\psi_{\nu_{n_2}}(\mathbf{r}_2)\ldots\psi_{\nu_{n_N}}(\mathbf{r}_N)|$ can be written as,

$$c^\dagger_{\nu_{n_1}} c^\dagger_{\nu_{n_2}} \cdots c^\dagger_{\nu_{n_N}} |0\rangle \tag{3.11}$$

where v_{n_j} denotes the occupied single-particle state in the N-particle system. The fermion creation and annihilation operators are defined to satisfy the following anti-commutation relations in accordance with the Pauli exclusion principle:

$$\{c^\dagger_{\nu_j}, c^\dagger_{\nu_k}\} = 0, \tag{3.12}$$

$$\{c_{\nu_j}, c_{\nu_k}\} = 0, \tag{3.13}$$

$$\{c_{\nu_j}, c^\dagger_{\nu_k}\} = \delta_{\nu_j\nu_k}, \tag{3.14}$$

where the anti-commutator $\{A, B\}$ for operators A and B is defined as,

$$\{A, B\} = AB + BA. \tag{3.15}$$

In terms of the creation and annihilation operators and their anti-commutation relations, the one- and two-particle operators can be written in second quantization form:

$$T_{\text{tot}} = \sum_{\nu_i\nu_j} T_{\nu_i\nu_j} c^\dagger_{\nu_i} c_{\nu_j}, \tag{3.16}$$

$$V_{\text{tot}} = \frac{1}{2} \sum_{\substack{\nu_i\nu_j \\ \nu_k\nu_l}} V_{\nu_i\nu_j;\nu_k\nu_l} c^\dagger_{\nu_i} c^\dagger_{\nu_k} c_{\nu_l} c_{\nu_j} \tag{3.17}$$

3.2.3 Mean-field theory and Hartree-Fock approximation

In second quantization form, the full nonrelativistic Hamiltonian for a system of electrons can be written as,

$$\mathcal{H} = \sum_{\nu\mu} t_{\nu\mu} c^\dagger_\nu c_\mu + \sum_{\substack{\nu\mu \\ \nu'\mu'}} u(\nu\mu;\nu'\mu') c^\dagger_\nu c^\dagger_{\nu'} c_{\mu'} c_\mu, \tag{3.18}$$

where ν, μ are basis states. The interaction between electrons is very complicated because not only the number of electrons can be large but also the motions of electrons are

correlated. The mean-field approximation assumes that a single particle is correlated with a mean field provided by other particles. Hartree-Fock approximation is a mean-field version, simplifying a four-term as,

$$\begin{aligned} c_\nu^\dagger c_{\nu'}^\dagger c_{\mu'} c_\mu \approx & \Big[c_\nu^\dagger c_\mu \langle c_{\nu'}^\dagger c_{\mu'} \rangle + c_{\nu'}^\dagger c_{\mu'} \langle c_\nu^\dagger c_\mu \rangle - \langle c_\nu^\dagger c_\mu \rangle \langle c_{\nu'}^\dagger c_{\mu'} \rangle \Big] \\ & - \Big[c_\nu^\dagger c_{\mu'} \langle c_{\nu'}^\dagger c_\mu \rangle + c_{\nu'}^\dagger c_\mu \langle c_\nu^\dagger c_{\mu'} \rangle - \langle c_\nu^\dagger c_{\mu'} \rangle \langle c_{\nu'}^\dagger c_\mu \rangle \Big]. \end{aligned} \tag{3.19}$$

Wick's theorem [48] states that a four-term expectation value can be factorized into two-term averages,

$$\langle c_\nu^\dagger c_{\nu'}^\dagger c_{\mu'} c_\mu \rangle = \langle c_\nu^\dagger c_\mu \rangle \langle c_{\nu'}^\dagger c_{\mu'} \rangle - \langle c_\nu^\dagger c_{\mu'} \rangle \langle c_{\nu'}^\dagger c_\mu \rangle \tag{3.20}$$

We can see that the Hartree-Fock approximation obeys the Wick's theorem.

Within the Hartree-Fock approximation, the final mean-filed Hamiltonian is

$$\mathcal{H}_{\mathrm{HF}} = \sum_{\nu\mu} t_{\nu\mu} c_\nu^\dagger c_\mu + V^{\mathrm{Hartree}} + V^{\mathrm{Fock}} \tag{3.21}$$

where

$$V^{\mathrm{Hartre}} = \frac{1}{2} \sum u(\nu\mu;\nu'\mu') \Big(c_\nu^\dagger c_\mu \langle c_{\nu'}^\dagger c_{\mu'} \rangle + c_{\nu'}^\dagger c_{\mu'} \langle c_\nu^\dagger c_\mu \rangle - \langle c_\nu^\dagger c_\mu \rangle \langle c_{\nu'}^\dagger c_{\mu'} \rangle \Big) \tag{3.22}$$

$$V^{\mathrm{Fock}} = -\frac{1}{2} \sum u(\nu\mu;\nu'\mu') \Big(c_\nu^\dagger c_{\mu'} \langle c_{\nu'}^\dagger c_\mu \rangle + c_{\nu'}^\dagger c_\mu \langle c_\nu^\dagger c_{\mu'} \rangle - \langle c_\nu^\dagger c_{\mu'} \rangle \langle c_{\nu'}^\dagger c_\mu \rangle \Big). \tag{3.23}$$

The HF energy is therefore written as,

$$E_{\mathrm{HF}} = \sum_{\nu\mu} t_{\nu\mu} \langle c_\nu^\dagger c_\mu \rangle + \frac{1}{2} \sum u(\nu\mu;\nu'\mu') \left[\langle c_\nu^\dagger c_\mu \rangle \langle c_{\nu'}^\dagger c_{\mu'} \rangle - \langle c_\nu^\dagger c_{\mu'} \rangle \langle c_{\nu'}^\dagger c_\mu \rangle \right] \tag{3.24}$$

3.3 CMR formalism

In principle, the Hohenberg-Kohn density functional should yield correct ground-state density and total energy for any electron system, including strongly correlated electron systems. In our view [37], the approximation in KS-DFT framework, which chooses noninteracting electron as the reference system, accounts for the failure at systems containing strongly electron correlation. To avoid such problem, we adopted Gutzwiller

wavefunction (GWF) and Gutzwiller approximation in DFT+Gutzwiller approximation [37–42] to evaluate one-body density matrix. Later in the CMR method [9], we further utilized the Gutzwiller approximation to evaluate the two-body operators in terms of noninteracting one-particle density matrix with renormalization factors.

Many-body Hamiltonian

The model Hamiltonian is commonly written as the sum of local and nonlocal parts:

$$\mathcal{H} = \sum_i \mathcal{H}_{i,\mathrm{loc}} + \mathcal{H}_{\mathrm{nonloc}} \tag{3.25}$$

where i is the site index.

The local part $\mathcal{H}_{i,loc}$ at site i can be written in the form of second quantization as

$$\mathcal{H}_{i,loc} = \sum_{\alpha\beta} t_{i\alpha i\beta} c^\dagger_{i\alpha\sigma} c_{i\beta\sigma} + \sum_{\alpha\beta\gamma\delta,\sigma\sigma'} u(i\alpha i\beta; i\gamma i\delta) c^\dagger_{i\alpha\sigma} c^\dagger_{i\beta\sigma'} c_{i\delta\sigma'} c_{i\gamma\sigma}. \tag{3.26}$$

Here the α, β, γ, δ are orbital indices, and σ, σ' are the spin indices. The coefficient t is the one-electron hopping integral defined as,

$$t_{i\alpha j\beta} = \langle \phi_{i\alpha} | \hat{T} + \hat{V}_{\mathrm{ion}} | \phi_{j\beta} \rangle, \tag{3.27}$$

which is the expectation value of kinetic energy operator $\hat{T}$ and electron-ion interaction operator $\hat{V}_{\mathrm{ion}}$. Here u is the two-electron Coulomb integral defined as,

$$u(i\alpha j\beta; k\gamma l\delta) = \int d\mathbf{r} \int d\mathbf{r}' \phi^*_{i\alpha}(\mathbf{r}) \phi^*_{j\beta}(\mathbf{r}') \hat{U}(|\mathbf{r} - \mathbf{r}'|) \phi_{l\delta}(\mathbf{r}') \phi_{k\gamma}(\mathbf{r}) \tag{3.28}$$

with $\hat{U}(|\mathbf{r} - \mathbf{r}'|) = \frac{1}{|\mathbf{r} - \mathbf{r}'|}$.

In Eq. 3.25, the nonlocal term containing contributions from nonlocal one-body and two-body interactions is given by,

$$\mathcal{H}_{\mathrm{nonloc}} = \sum_{i\alpha j\beta,\sigma}{}' t_{i\alpha j\beta} c^\dagger_{i\alpha\sigma} c_{j\beta\sigma} + \frac{1}{2} \sum_{\substack{i\alpha j\beta \\ k\gamma l\delta,\sigma\sigma'}}{}' u(i\alpha j\beta; k\gamma l\delta) c^\dagger_{i\alpha\sigma} c^\dagger_{j\beta\sigma'} c_{l\delta\sigma'} c_{k\gamma\sigma} \tag{3.29}$$

where $\sum'$ means that the pure local on-site terms ($i = j$ for one-body part and $i = j = k = l$ for two-body part) are excluded from the summation.

Gutzwiller wavefunction

The GWF was first introduced by Gutzwiller [16] to study ferromagnetism in one-band Hubbard model. The basic idea is to construct GWF by starting from uncorrelated state and to reduce the probability of doubly occupied states. The GWF of an interacting system is constructed from wavefunction $|\Psi_0\rangle$ of the noninteracting system by Gutzwiller correlator $\hat{P}_G$, being expressed as,

$$\begin{aligned} |\Psi_G\rangle &= \hat{P}_G |\Psi_0\rangle \\ \hat{P}_G &\equiv \prod_i \left(\sum_\Gamma g_{i\Gamma} |\Gamma_i\rangle \langle \Gamma_i| \right), \end{aligned} \tag{3.30}$$

where $g_{i\Gamma}$ is the Gutzwiller variational parameter of the local atomic eigenstates $|\Gamma_i\rangle$ on site i, being chosen to minimize the ground-state total energy. Note that if the local Hamiltonian includes only density-density interaction, it is also possible to choose Slater determinants as local configurations since the density-density Hamiltonian is diagonal, but it is better to choose the local eigenstates instead of spin-orbit product state when we consider realistic situations and also symmetry requirements [17].

For any operator $\mathcal{O}$ and wavefunction $|\Psi_X\rangle$, we now define a short-hand notation:

$$\langle \mathcal{O} \rangle_{\mathrm{X}} \equiv \langle \Psi_X | \mathcal{O} | \Psi_X \rangle. \tag{3.31}$$

Here $|\Psi_X\rangle$ can be the Gutzwiller wavefunction $|\Psi_G\rangle$, the uncorrelated wavefunction $|\Psi_0\rangle$, or the wavefunction $|\Psi_{\mathrm{FCI}}\rangle$ from the full configuration interaction (FCI) method.

In the CMR framework, we adopt the GWF to evaluate the many-body Hamiltonian since the GWF can take care of the dominant local electron correlations. Given the eigenstates $\{\Gamma_i\}$ of the local onsite many-body Hamiltonian, the spectral representation of $\mathcal{H}_{i,loc}$ can be written as,

$$\sum_i \mathcal{H}_{i,\mathrm{loc}} = \sum_{i\Gamma} E_{i\Gamma} |\Gamma_i\rangle \langle \Gamma_i| \tag{3.32}$$

where $E_{i\Gamma}$ is the corresponding energy for the local configuration $|\Gamma_i\rangle$, and the total energy evaluated by the CMR approximation becomes,

$$\begin{aligned} E_{\mathrm{CMR}} = & \sum_{i\Gamma} p_{i\Gamma} E_{i\Gamma} + \sum_{i\alpha j\beta,\sigma}{}' t_{i\alpha j\beta} \left\langle c^\dagger_{i\alpha\sigma} c_{j\beta\sigma} \right\rangle_{\mathrm{CMR}} \\ & + \frac{1}{2} \sum_{\substack{i\alpha j\beta \\ k\gamma l\delta,\sigma\sigma'}}{}' u(i\alpha j\beta; k\gamma l\delta) \left\langle c^\dagger_{i\alpha\sigma} c^\dagger_{j\beta\sigma'} c_{l\delta\sigma'} c_{k\gamma\sigma} \right\rangle_{\mathrm{CMR}} \end{aligned} \tag{3.33}$$

where $p_{i\Gamma}$ is the occupation probability of $|\Gamma_i\rangle$.

Approximation for nonlocal one-electron part

The second term in Eq. 3.33, the local one-electron part, can be evaluated with the approximated nonlocal one-electron density matrix (1PDM), which is the idea of Gutzwiller approximation [16, 17, 49]. Then the one-electron term can be approximated as,

$$\left\langle c^\dagger_{i\alpha\sigma} c_{j\beta\sigma} \right\rangle_{\mathrm{CMR}} \approx z^{j\beta}_{i\alpha\sigma} \left\langle c^\dagger_{i\alpha\sigma} c_{j\beta\sigma} \right\rangle_0 . \tag{3.34}$$

Here $z^{j\beta}_{i\alpha\sigma}$ is defined as

$$z^{j\beta}_{i\alpha\sigma} \equiv \begin{cases} z_{i\alpha\sigma} z_{j\beta\sigma} & \text{if } i\alpha \neq j\beta \\ 1 & \text{otherwise} \end{cases} \tag{3.35}$$

with the one-electron renormalization factor $z_{i\alpha\sigma}$.

The most general form of the $z_{i\alpha\sigma}$ is complicated [50]. Nevertheless, the form is much simpler and manageable when the local onsite eigenstates $\{\Gamma\}$ are identical with Fock states $\{\mathcal{F}\}$. This condition exists for single-orbital systems like hydrogen molecules with minimal basis set, and also holds approximately if the classical Coulomb interaction and exchange integrals are dominant in local Hamiltonian. The z-factor is then written as,

$$z^{GA}_{i\alpha\sigma} = \sum_{\mathcal{F}\mathcal{F}'} \frac{\sqrt{p_{i\mathcal{F}} p_{i\mathcal{F}'}} |\langle \mathcal{F}_i | c^\dagger_{i\alpha\sigma} | \mathcal{F}'_i \rangle|}{\sqrt{n^0_{i\alpha\sigma}(1 - n^0_{i\alpha\sigma})}}. \tag{3.36}$$

Here, $n^0_{i\alpha\sigma}$ is the expectation value of occupation operator with $|\Psi_0\rangle$, given by,

$$n^0_{i\alpha\sigma} = \langle c^\dagger_{i\alpha\sigma} c_{i\alpha\sigma} \rangle_0 \equiv \langle \Psi_0 | \, c^\dagger_{i\alpha\sigma} c_{i\alpha\sigma} \, | \Psi_0 \rangle . \tag{3.37}$$

The redefined variational parameters $\{p_{i\mathcal{F}}\}$ are occupation probabilities of Fock states $|\mathcal{F}_i\rangle$. A Fock state can be generated by applying creation operator on vacuum state. We can use the occupation number $n^{\mathcal{F}}_{i\alpha\sigma}$ (0 or 1) to indicate whether the spin-orbital state $i\alpha\sigma$ is occupied or not in Fock state $|\mathcal{F}_i\rangle$:

$$|\mathcal{F}_i\rangle = \prod_{\alpha\sigma}(c^\dagger_{i\alpha\sigma})^{n^{\mathcal{F}}_{i\alpha\sigma}}|0\rangle, \tag{3.38}$$

The work presented here focuses mostly on molecules, so the above form of z-factor is used for simplicity, i.e., the form is presented with the Fock states from now on.

Approximation for nonlocal two-electron part

The evaluation for the third term in Eq. 3.33 remains difficult with the GWF, in that the two-electron density matrix or correlation matrix (2PCM) $\left\langle c^\dagger_{i\alpha\sigma}c^\dagger_{j\beta\sigma'}c_{l\delta\sigma'}c_{k\gamma\sigma}\right\rangle_{\text{CMR}}$ needs be approximated. The generalized GA scheme introduces Gutzwiller renormalization factors $z_{c^\dagger_{i\alpha\sigma}c^\dagger_{j\beta\sigma'}c_{l\delta\sigma'}c_{k\gamma\sigma}}$ to evaluate the expectation of two-electron operator, but this renormalization factor is not completely factorizable. In the CMR method, we assume that the Wick's theorem still holds, and then the two-electron term can be factorized like HF method with additional renormalizations:

$$\begin{aligned}\left\langle c^\dagger_{i\alpha\sigma}c^\dagger_{j\beta\sigma'}c_{l\delta\sigma'}c_{k\gamma\sigma}\right\rangle_{\text{CMR}} =& z^{k\gamma}_{i\alpha\sigma}z^{l\delta}_{j\beta\sigma'}\left\langle c^\dagger_{i\alpha\sigma}c_{k\gamma\sigma}\right\rangle_0\left\langle c^\dagger_{j\beta\sigma'}c_{l\delta\sigma'}\right\rangle_0 \\ &- \delta_{\sigma\sigma'}z^{l\delta}_{i\alpha\sigma}z^{k\gamma}_{j\beta\sigma}\left\langle c^\dagger_{i\alpha\sigma}c_{l\delta\sigma}\right\rangle_0\left\langle c^\dagger_{j\beta\sigma}c_{k\gamma\sigma}\right\rangle_0 .\end{aligned} \tag{3.39}$$

Note that if the renormalization factor is equal to one, then the expectation of two-electron operator is identical with the Hartree and exchange terms in HF method. Therefore, the CMR method renormalizes both the one-electron and two-electron density matrix from the mean-field HF values by renormalization z-factors. Now with the CMR approximations, the total energy can be written as,

$$
\begin{aligned}
E_{\mathrm{CMR}} = & \sum_{i\Gamma} p_{i\Gamma} E_{i\Gamma} + \sum_{i\alpha j\beta,\sigma}{}' t_{i\alpha j\beta} z_{i\alpha\sigma}^{j\beta} \left\langle c_{i\alpha\sigma}^{\dagger} c_{j\beta\sigma} \right\rangle_0 \\
& + \frac{1}{2} \sum_{\substack{i\alpha j\beta \\ k\gamma l\delta,\sigma\sigma'}}{}' u(i\alpha j\beta; k\gamma l\delta) \Bigg[z_{i\alpha\sigma}^{k\gamma} z_{j\beta\sigma'}^{l\delta} \left\langle c_{i\alpha\sigma}^{\dagger} c_{k\gamma\sigma} \right\rangle_0 \left\langle c_{j\beta\sigma'}^{\dagger} c_{l\delta\sigma'} \right\rangle_0 \\
& - \delta_{\sigma\sigma'} z_{i\alpha\sigma}^{l\delta} z_{j\beta\sigma}^{k\gamma} \left\langle c_{i\alpha\sigma}^{\dagger} c_{l\delta\sigma} \right\rangle_0 \left\langle c_{j\beta\sigma}^{\dagger} c_{k\gamma\sigma} \right\rangle_0 \Bigg].
\end{aligned}
\tag{3.40}
$$

3.4 Reducing errors introduced by CMR approximation

If the CMR total energy shown in Eq. 3.40 is compared with the FCI one given by

$$
\begin{aligned}
E_{\mathrm{FCI}} = & \sum_{i\Gamma} p_{i\Gamma} E_{i\Gamma} + \sum_{i\alpha j\beta,\sigma}{}' t_{i\alpha j\beta} \left\langle c_{i\alpha\sigma}^{\dagger} c_{j\beta\sigma} \right\rangle_{\mathrm{FCI}} \\
& + \frac{1}{2} \sum_{\substack{i\alpha j\beta \\ k\gamma l\delta,\sigma\sigma'}}{}' u(i\alpha j\beta; k\gamma l\delta) \left\langle c_{i\alpha\sigma}^{\dagger} c_{j\beta\sigma'}^{\dagger} c_{l\delta\sigma'} c_{k\gamma\sigma} \right\rangle_{\mathrm{FCI}},
\end{aligned}
\tag{3.41}
$$

it can be seen that they have the same form of the first term. The equality is as expected since the CMR method utilizes the GWF to treat the local onsite terms exactly.

However, in the evaluation of the nonlocal one-electron and two-electron terms, the CMR method inevitably introduces errors with the approximations. Two key issues need be considered when we want to apply the CMR approach in real systems. The first one is the form of the z-factor in finite dimensions. The standard z-factor in GA shown above is only exact in infinite dimension, while the best form in finite dimensions (e.g., 0, 1, 2 or 3 dimensions) is complicated [50]. The second concern is whether the Wick's theorem remains valid for GWF. The answer is that it does not hold true. That is why the factorization of the 2PCM through CMR approach introduces additional errors, thereby violating sum rules, i.e.,

$$
\sum_{\beta\sigma'} \langle \hat{n}_{\alpha\sigma} \hat{n}_{\beta\sigma'} \rangle_{\mathrm{CMR}} \neq N_e \langle \hat{n}_{\alpha\sigma} \rangle_{\mathrm{CMR}}. \tag{3.42}
$$

One way to evaluate the two issues is to examine the CMR behavior in a analytically solvable model. Comparing the exact result and CMR in the case of hydrogen dimer with minimal basis, we found two approaches to reduce the errors.

3.4.1 Analytical expression for H_2 with minimal basis

In the case of H_2 with minimal basis set, the analytical expression for total energies can be obtained [9] through different methods, like HF, CMR and Gutzwiller variational method. The variational approach with GWF can produce exact result. Therefore it is possible to find the differences between the CMR method and the exact result, which indicates two approaches to reduce the approximation errors.

In the H_2 system with minimal basis set, one hydrogen atom has only one spatial orbital. The Hamiltonian is then written as [9],

$$\begin{aligned}\mathcal{H} = &\sum_{i=1}^{2}\left(\sum_{\sigma}\epsilon c_{i\sigma}^{\dagger}c_{i\sigma} + \frac{1}{2}\sum_{\sigma\sigma'}u_0 c_{i\sigma}^{\dagger}c_{i\sigma'}^{\dagger}c_{i\sigma'}c_{i\sigma}\right)\\ &-\sum_{\sigma}t(c_{1\sigma}^{\dagger}c_{2\sigma} + \text{H.C.})\\ &+\frac{1}{2}\sum_{i,j=1}^{2\prime}\sum_{\sigma\sigma'}u_1(c_{i\sigma}^{\dagger}c_{i\sigma'}^{\dagger}c_{i\sigma'}c_{j\sigma} + c_{i\sigma}^{\dagger}c_{i\sigma'}^{\dagger}c_{j\sigma'}c_{i\sigma} + c_{i\sigma}^{\dagger}c_{j\sigma'}^{\dagger}c_{i\sigma'}c_{i\sigma} + c_{j\sigma}^{\dagger}c_{i\sigma'}^{\dagger}c_{i\sigma'}c_{i\sigma})\\ &+\frac{1}{2}\sum_{i,j=1}^{2\prime}\sum_{\sigma\sigma'}u_2(c_{i\sigma}^{\dagger}c_{i\sigma'}^{\dagger}c_{j\sigma'}c_{j\sigma} + c_{i\sigma}^{\dagger}c_{j\sigma'}^{\dagger}c_{i\sigma'}c_{j\sigma}) + \frac{1}{2}\sum_{i,j=1}^{2\prime}\sum_{\sigma\sigma'}u_3(c_{i\sigma}^{\dagger}c_{j\sigma'}^{\dagger}c_{j\sigma'}c_{i\sigma}),\end{aligned} \tag{3.43}$$

where the symbols are defined as integrals using the notations in Eq. 3.27 and 3.28:

$$-t = t_{1\sigma,2\sigma} \tag{3.44}$$

$$u_0 = u(11;11) \tag{3.45}$$

$$u_1 = u(11;12) \tag{3.46}$$

$$u_2 = u(11;22) \tag{3.47}$$

$$u_3 = u(12;12). \tag{3.48}$$

They also have physical contents: $-t$ is the one-electron inter-site hopping integral, ϵ is the $1s$ energy level, u_0 is the onsite classical Coulomb interaction, u_2 is the inter-site exchange integral, and u_3 is the inter-site classical Coulomb interaction.

HF For the HF method, the molecular wavefunction for H_2 is well-known, written as,

$$\psi_\sigma = \frac{1}{\sqrt{2}}\left(\phi_{1s\sigma} + \phi_{2s\sigma}\right). \tag{3.49}$$

Therefore, the non-interacting ground state wavefunction is written as,

$$|\Psi_0\rangle = \frac{1}{\sqrt{2}}\left(c^\dagger_{1\uparrow}|0\rangle + c^\dagger_{2\uparrow}|0\rangle\right)\frac{1}{\sqrt{2}}\left(c^\dagger_{1\downarrow}|0\rangle + c^\dagger_{2\downarrow}|0\rangle\right). \tag{3.50}$$

The expectation of Hamiltonian in Eq. 3.43 is then given by,

$$\begin{aligned} E_{HF} &= \langle\Psi_0|\mathcal{H}|\Psi_0\rangle \\ &= \left(2\epsilon + \frac{1}{2}u_0\right) - 2t + 2u_1 + u_2 + \frac{1}{2}u_3. \end{aligned} \tag{3.51}$$

GWF In the Gutzwiller variational method, there are four local eigenstates for each hydrogen atom:

$$\{|\mathcal{F}\rangle\} = \{|0\rangle,\, |\uparrow\rangle,\, |\downarrow\rangle,\, |\uparrow\downarrow\rangle\}. \tag{3.52}$$

According to symmetry, the corresponding variational parameters have the following equalities:

$$\begin{aligned} g_{1|0\rangle} &= g_{2|0\rangle} = g_{1|\uparrow\downarrow\rangle} = g_{2|\uparrow\downarrow\rangle} \equiv g_0 \\ g_{1|\uparrow\rangle} &= g_{2|\uparrow\rangle} = g_{1|\downarrow\rangle} = g_{2|\downarrow\rangle} \equiv g_1 \end{aligned} \tag{3.53}$$

Following the definition in Eq. 3.30, the GWF can then be written as,

$$\begin{aligned} |\Psi_{\mathrm{GWF}}\rangle &= \prod_i^2 \left(\sum_\Gamma g_{i\Gamma}\,|\Gamma_i\rangle\,\langle\Gamma_i|\right)|\Psi_0\rangle \Big/ \langle\Psi_0|\hat{P}^\dagger_G\hat{P}_G|\Psi_0\rangle \\ &= \prod_i^2 \left[g_0\Big(|0\rangle\langle 0| + |\uparrow\downarrow\rangle\langle\uparrow\downarrow|\Big) + g_1\Big(|\uparrow\rangle\langle\uparrow| + |\downarrow\rangle\langle\downarrow|\Big)\right]|\Psi_0\rangle \Big/ \langle\Psi_0|\hat{P}^\dagger_G\hat{P}_G|\Psi_0\rangle \\ &= \sqrt{d}\left(c^\dagger_{1\uparrow}c^\dagger_{1\downarrow}|0\rangle + c^\dagger_{2\uparrow}c^\dagger_{2\downarrow}|0\rangle\right) + \sqrt{\frac{1}{2} - d}\left(c^\dagger_{1\uparrow}c^\dagger_{2\downarrow}|0\rangle + c^\dagger_{1\downarrow}c^\dagger_{2\uparrow}|0\rangle\right). \end{aligned} \tag{3.54}$$

where $d = g_0^4/(2(g_0^4+g_1^4))$ is the double occupancy $p_{i|\uparrow\downarrow\rangle}$, that is, the occupation probability of two electrons on one site. Accordingly, the GWF energy in terms of d is expressed as [9],

$$E_{GWF}(d) = 2\epsilon + 2du_0 + 8\sqrt{d(\frac{1}{2}-d)}(-t+u_1) + u_2 + (1-2d)u_3. \tag{3.55}$$

Through variational method with respect to d, the ground state energy can be given by,

$$E_{GWF} = 2\epsilon + \frac{1}{2}u_0 + u_2 + \frac{1}{2}\left(u_3 - \sqrt{16(-t+u)^2 + (u_0-u_3)^2}\right). \tag{3.56}$$

At the same time, the z_{GA} factor used in GA approximations can also be determined in this case. For $\langle n_{1\sigma}^0\rangle = 1/2$, $p_{i|0\rangle} = p_{i|\uparrow\downarrow\rangle} = d$ and $p_{i|\uparrow\rangle} = p_{i|\downarrow\rangle} = 1/2 - d$, the z_{GA} factor is written as,

$$\begin{aligned} z_{GA} &= \frac{\sqrt{p_{1|\uparrow\downarrow\rangle}p_{1|\downarrow\rangle}}|\langle\uparrow\downarrow|c_{1\uparrow}^\dagger|\downarrow\rangle| + \sqrt{p_{1|\uparrow\rangle}p_{1|0\rangle}}|\langle\uparrow|c_{1\uparrow}^\dagger|0\rangle|}{\sqrt{n_{i\alpha\sigma}^0(1-n_{i\alpha\sigma}^0)}} \\ &= 4\sqrt{d(\frac{1}{2}-d)}. \end{aligned} \tag{3.57}$$

Therefore, the coefficient ahead of the $(-t+u_1)$ is equal to $2z_{GA}$, like [9]:

$$E_{GWF} = 2\epsilon + 2du_0 + 2z_{GA}(-t+u_1) + u_2 + (1-2d)u_3. \tag{3.58}$$

CMR Following Eq. 3.40, we can obtain the total energy evaluation in the CMR method [9], given by,

$$E_{CMR} = 2\epsilon + 2du_0 + 2z^2(-t+u_1) + \frac{1}{2}(3z^4-1)u_2 + (1-z^4/2)u_3. \tag{3.59}$$

The details are lengthy, so only a few examples of evaluations are listed here:

$$\epsilon\langle c_{1\uparrow}^\dagger c_{1\uparrow}\rangle_{CMR} = (p_{1|\uparrow\rangle} + p_{1|\uparrow\downarrow\rangle})\epsilon = \frac{1}{2}\epsilon$$

$$u_0\langle c_{1\uparrow}^\dagger c_{1\downarrow}^\dagger c_{1\downarrow}c_{1\uparrow}\rangle_{CMR} = u_0 p_{1|\uparrow\downarrow\rangle} = du_0$$

$$
\begin{aligned}
-t\langle c^\dagger_{1\uparrow}c_{2\downarrow}\rangle_{CMR} =&(-t)z^2\langle c^\dagger_{1\uparrow}c_{2\downarrow}\rangle_0 = \frac{z^2}{4}(-t)\\
u_1\langle c^\dagger_{1\uparrow}c^\dagger_{1\downarrow}c_{1\downarrow}c_{2\uparrow}\rangle_{CMR} =&u_1 z^{2\uparrow}_{1\uparrow}z^{1\downarrow}_{1\downarrow}\langle c^\dagger_{1\uparrow}c_{2\uparrow}\rangle_0\langle c^\dagger_{1\downarrow}c_{1\downarrow}\rangle_0\\
=&u_1 z^2(\frac{1}{2})(\frac{1}{2})\\
u_2\langle c^\dagger_{1\uparrow}c^\dagger_{2\uparrow}c_{1\uparrow}c_{2\uparrow}\rangle_{CMR} =&u_2\Big(z^{2\uparrow}_{1\uparrow}z^{1\uparrow}_{2\uparrow}\langle c^\dagger_{1\uparrow}c_{2\uparrow}\rangle_0\langle c^\dagger_{2\uparrow}c_{1\uparrow}\rangle_0\\
&- z^{1\uparrow}_{1\uparrow}z^{2\uparrow}_{2\uparrow}\langle c^\dagger_{1\uparrow}c_{1\uparrow}\rangle_0\langle c^\dagger_{2\uparrow}c_{2\uparrow}\rangle_0\Big)\\
=&u_2\Big(z^2(\frac{1}{2})(\frac{1}{2}) - (\frac{1}{2})(\frac{1}{2})\Big).
\end{aligned}
$$

3.4.2 The form of z-factor and sum rules

We studied the form of the z-factors in our early work and proposed a functional form $f(z)$ [10] during the renormalization of the 1PDM and 2PCM. This scheme is performed well on small molecules, such as hydrogen clusters H_n, nitrogen clusters N_n, and ammonia NH_3. The disadvantage within this approach is that the functional $f(z)$ is not analytically available. The functional can only be parametrized through fitting to exact results. For example, the functional $f(z)$ used in calculations for hydrogen clusters H_n is obtained from fitting to total energy data of H_2 in which the exact total energies are presented as a function of bond length. It is desired to have a functional form $f(z)$ without fitting. The analytically solvable case to examine the functional form is the hydrogen dimer H_2. Despite that the system is simple, the electron correlation still has a transition from weak to strong as the bond length increases. The exact energy can be obtained through Gutzwiller variation approach as we have shown in Eq. 3.41. We rewrite the total energies here for comparison:

$$
\begin{aligned}
E_{\text{exact}} =&2\epsilon + 2du_0 + 2z_{GA}(-t+u_1)\\
&+ u_2 + u_3 - 2du_3,\\
E_{\text{CMR}} =&2\epsilon + 2du_0 + 2z^2(-t+u_1)\\
&+ \frac{1}{2}(3z^4-1)u_2 + u_3 - \frac{z^4}{2}u_3,
\end{aligned}
\tag{3.60}
$$

where the symbols hold their meanings. Note that in general the two-body integrals hold the relation: $u_0 > u_3 \gg u_2 > u_1$.

The exact result and CMR energy both show indeed the same on-site treatment. Besides, the limiting behavior of the CMR approach is also correct. At small separation where $d \to 1/4$ and $z, z_{GA} \to 1$, the CMR energy is expressed by,

$$E = 2\epsilon + \frac{1}{2}u_0 + 2(-t + u_1) + u_2 + \frac{1}{2}u_3. \tag{3.61}$$

which is the same with exact result. At large separation limit where $d, z, z_{GA} \to 0$ and $u_2, u_3 \to 0$, the CMR also shows correct atomic limit of

$$E = 2\epsilon. \tag{3.62}$$

In the intermediate range where the bond breaking phenomenon happens, there are still deviations though.

For terms including t and u_1 in Eq. 3.60, a simple square root transformation of the z-factor, i.e., $z = \sqrt{z_{GA}}$, can help the CMR method match the corresponding part of the exact result. However, the term including inter-site Coulomb interaction u_3, which contributes significantly to the total energy, still remains different. Fortunately, sum-rule terms can reorganize the Coulomb contributions into the local onsite part that is treated accurately in the CMR approach. In addition to the original Hamiltonian of H_2, the sum-rule Hamiltonian is given by,

$$\mathcal{H}_{s.r.} = \frac{1}{2}\sum_{i=1}^{2}\sum_{\sigma}(-u_3)\hat{n}_{i\sigma}\left(\sum_{j=1}^{2}\sum_{\sigma'}\hat{n}_{j\sigma'} - N_e\right). \tag{3.63}$$

Note that the additional sum-rule Hamiltonian does not change the total energy, since the expectation value of such term always remains zero with respect to many-body wave functions. However, the two-electron density matrix approximation in the CMR method violates the sum rules. The good thing is that onsite evaluations in the CMR are accurate. Therefore the sum-rule terms help reduce the approximation errors by shifting

the inter-site Coulomb terms into local onsite evaluations. As a result, the CMR total energy with the sum rules can be expressed by,

$$E_{\mathrm{CMR}} = E_{\mathrm{exact}} + \frac{3}{2}(z_{GA}^2 - 1)u_2. \tag{3.64}$$

There is still a residual term including inter-site exchange integral u_2, but the contribution of such term is relatively very small. The reasons are that u_2 is much smaller than u_0 and u_3, and that u_2 decays much fast when separation of atoms is increasing. Besides, this term will also vanish at small atomic separation where z_{GA} is approaching unity.

The sum-rule terms in H_2 case completely cancel the inter-site Coulomb interactions. Nevertheless, such scheme is unable to work perfectly when extended to general multi-orbital molecular systems. In order to shift the inter-site interactions as much as possible, we introduce the following sum-rule correction for general cases:

$$\mathcal{H}_{s.r.} = \frac{1}{2}\sum_{i\alpha} \lambda_{i\alpha\sigma}\Big(\hat{n}_{i\alpha\sigma}\Big(\sum_{j\beta\sigma'} \hat{n}_{j\beta\sigma'} - N_e\Big)\Big) \tag{3.65}$$

with the prefactor $\lambda_{i\alpha}$ defined as

$$\lambda_{i\alpha} = -\frac{\sum_{j\neq i,\beta\sigma'} u(i\alpha j\beta; i\alpha j\beta) R_{ij}^{-6}}{\sum_{j\neq i,\beta\sigma'} R_{ij}^{-6}} \tag{3.66}$$

where R_{ij} is the distance from atom j to atom i. Note that the $\lambda_{i\alpha}$ is actually the weighted average of the inter-site two-electron Coulomb integrals with weighting factor set as R_{ij}^{-6}. Such form is only derived from practical convenience. The power index six can limit the interactions to be considered only within a small range of the orbital α at atom i, which is reasonable because the inter-site interaction decays fast. The determination of λ is certainly not unique, and a sophisticated approach can be referenced in the supporting material of our published article [11].

3.5 Construction of quasi-atomic minimal-basis-set orbitals

If we want to apply the CMR method into real systems and compare the results with experimental data or exact quantum chemistry results, one concern is the selection of

basis set. In principle, a larger basis set is supposed to provide more accurate result, but the quantum calculation with large basis set is demanding. In our work, we utilized the quasi-atomic minimal-basis-set orbitals (QUAMBO) developed previously by our group [18, 19]. Here a detailed formalism is presented for construction of QUAMBO under the scheme of CMR method.

Formulation

The basis set is denoted as $|\phi_i\rangle$, which is not necessarily orthonormal. The overlap matrix is then defined as $S_{ij} = \langle\phi_i|\phi_j\rangle$. Molecular orbital (MO) from self-consistent-field (SCF) calculations, like the Hartree-Fock method or DFT, is denoted as ψ_i, which is expanded by basis orbitals as,

$$|\psi_i\rangle = \sum_j |\phi_j\rangle M_{ji}. \tag{3.67}$$

The orthonormal condition should hold true, given by

$$\begin{aligned}\langle\psi_i|\psi_j\rangle &= \left(\sum_m M^*_{mi}\langle\phi_m|\right)\left(\sum_n M_{nj}|\phi_n\rangle\right)\\ &= \sum_{m,n} M^\dagger_{im} S_{mn} M_{nj}\\ &= (M^\dagger S M)_{ij}\\ &= \delta_{ij}.\end{aligned} \tag{3.68}$$

The SCF MOs can be divided into two parts: one part has N_{occ} occupied MOs denoted as ψ^{occ} with expansion coefficients M_{occ}, and the other part has N_v unoccupied MOs denoted as ψ^v with expansion coefficients M_v. The atomic orbitals (AO) of free atoms are also expanded by basis, expressed as,

$$\varphi_i = \sum_j |\phi_j\rangle A_{ji}. \tag{3.69}$$

Here the number of free-atomic AOs is the same as the number of QUAMBOs, denoted as N. Usually, N_{occ} is smaller than or equal to N.

The problem of finding the QUAMBOs is to recover a set of deformed quasi-atomic orbitals from a space of occupied SCF MOs. The procedure can be broken down into the following steps:

1. Keep the occupied SCF MOs unchanged.

2. If we expand the AOs by SCF MOs, the expansion coefficients are given by,

$$C_{ij} = \sum_k \langle \varphi_i | \psi_k^{occ} \rangle \langle \psi_k^{occ} | \varphi_j \rangle, \tag{3.70}$$

$$C = (M^\dagger SA)^\dagger (M^\dagger SA). \tag{3.71}$$

   In the diagonalization of matrix C, eigenvectors φ^0 with eigenvalues zero consist of a space $\mathbb{C}_0$, which is orthogonal with respect to occupied SCF MOs in the space of free-atomic AOs. The expansion coefficients are denoted as C_0.

$$\varphi^0 = \phi C_0 \tag{3.72}$$

3. Find the projection of $\mathbb{C}_0$ in the unoccupied SCF MOs space consisting of ψ^v.

$$D_{ij} = \sum_k \langle \psi_i^v | \varphi_k^0 \rangle \langle \varphi_k^0 | \psi_j^v \rangle \tag{3.73}$$

$$D = (C_0^\dagger S M_v)^\dagger (C_0^\dagger S M_v) \tag{3.74}$$

   In the diagonalization of D, eigenvectors ψ^1 with eigenvalues one compose of a new space $\mathbb{D}_1$, which is expanded as

$$\psi^1 = \phi D_1. \tag{3.75}$$

4. The new subset $\mathbb{F}$ of SCF MO space is composed by $\tilde{\psi} \equiv (\psi^{occ}, \psi^1)$. The transformation matrix is written as,

$$F = (M_{occ}, D_1) \tag{3.76}$$

5. Find orbitals which are as similar as possible with the free-atomic AOs in subset $\mathbb{F}$ formed by SCF MO space,

$$\begin{aligned}\tilde{\varphi}_i &= \sum_k |\tilde{\psi}_k\rangle\langle\tilde{\psi}_k|\varphi_i\rangle \\ &= \sum_{k,j} |\phi_j\rangle F_{jk}(F^\dagger SA)_{ki} \\ &= \sum_j |\phi_j\rangle (FF^\dagger SA)_{ji},\end{aligned} \tag{3.77}$$

which are the QUAMBOs with expansion coefficients defined as,

$$\begin{aligned}\tilde{\varphi}_i &= \sum_j |\phi_j\rangle Q_{ji} \\ Q &= (FF^\dagger SA).\end{aligned} \tag{3.78}$$

In the implementation of CMR, the Hamiltonian integrals are firstly obtained by integration over basis sets. Then a rotation is required to have the Hamiltonian represented in the basis of QUAMBOs or SCF MOs. The Hamiltonian is composed of one-body part and two-body part:

$$\mathcal{H} = \mathcal{T} + \mathcal{V} \tag{3.79}$$

The integral for one-body operator expressed in basis set is defined as,

$$T_{ij} = \langle\phi_i|\mathcal{T}|\phi_j\rangle \tag{3.80}$$

If one wants to express it in QUAMBOs or SCF MOs, the matrix representation is given by,

$$\begin{aligned}\langle\psi_i|\mathcal{T}|\psi_j\rangle &= \sum_{m,n} M^*_{mi}\langle\phi_m|\mathcal{T}|\phi_n\rangle M_{nj} \\ &= (M^\dagger TM)_{ij} \\ T^\psi &= M^\dagger T^\phi M\end{aligned} \tag{3.81}$$

where T^{ψ} is the matrix representation of $\mathcal{T}$ in space composed of ψ. Similarly, the transformation is a high order tensor product for two-body part, given by,

$$\begin{aligned}\langle\psi_i(r)|\langle\psi_k(r')|\mathcal{U}|\psi_l(r')\rangle|\psi_j(r)\rangle &= \sum_{m,n,q,p} M^*_{mi}M^*_{qk}\langle\phi_m|\langle\phi_k|\mathcal{U}|\phi_p\rangle|\phi_n\rangle M_{pl}M_{nj} \\ U^{\psi}_{ij;kl} &= \sum_{m,n,q,p} M^{\dagger}_{im}M^{\dagger}_{kq}U^{\phi}_{mn;qp}M_{pl}M_{nj}\end{aligned} \tag{3.82}$$

Frozen core approximation

It is common in correlated calculations to invoke frozen core approximation, in which the lowest-lying orbitals (core orbitals) are constrained to remain doubly-occupied. The total energy and other physical quantities, are supposed to be insensitive to whether the core is frozen or not. However an issue exists in our construction of QUAMBOs, in which the lowest-lying QUAMBOs are constructed from the full SCF MOs. The core QUAMBOs are not supposed to be perfectly doubly-occupied, especially at small separation. Therefore, a practical way to solve this issue is to divide the QUAMBOs into core and valence parts, and the core QUAMBOs are constructed solely from lowest lying SCF MOs.

The frozen core approximation simplifies the expectation value of the full Hamitonian given in Eq. 3.18, in which some terms are evaluated directly and some two-body integrals are contracted into one-body integral:

$$\begin{aligned}\langle\mathcal{H}\rangle =& E_{fc} + \sum_{i\alpha,j\beta\in\mathcal{S}_v}\sum_{\sigma}\tilde{t}_{i\alpha i\beta}\langle c^{\dagger}_{i\alpha\sigma}c_{i\beta\sigma}\rangle \\ &+\frac{1}{2}\sum_{\substack{i\alpha,j\beta\in\mathcal{S}_v\\ k\gamma,l\delta\in\mathcal{S}_v}}\sum_{\sigma\sigma'}u(i\alpha j\beta;k\gamma l\delta)\langle c^{\dagger}_{i\alpha\sigma}c^{\dagger}_{j\beta\sigma'}c_{l\delta\sigma'}c_{k\gamma\sigma}\rangle\end{aligned} \tag{3.83}$$

where $\mathcal{S}_v$ is the subspace composed by valence orbitals, and E_{fc} is the energy contribution from core orbitals, given by

$$E_{fc} = \sum_{i\alpha\in\mathcal{S}_v} 2t_{i\alpha i\alpha} + \sum_{i\alpha,j\beta\in\mathcal{S}_v} 2\Big[u(i\alpha j\beta;i\alpha j\beta) - u(i\alpha j\beta;j\beta i\alpha)\Big]. \tag{3.84}$$

The one-electron integral in Eq. 3.83 includes not only the original one-electron integral but also the Coulomb interaction from two-body part, which is redefined as,

$$\tilde{t}_{i\alpha i\beta} = t_{i\alpha i\beta} + \sum_{k\gamma \in \mathcal{S}_v} \Big[2u(i\alpha k\gamma; j\beta k\gamma) - u(i\alpha k\gamma; k\gamma j\beta) \Big]. \tag{3.85}$$

3.6 Self-consistent loop

According to the factorization for two-electron density matrix, we can deduce the same form of one-electron equations as HF and DFT shown in Chapter 2. However, the self-consistent solver in the CMR method includes two loops: one is the equations with effective Hamiltonian and the other is the optimization for local configurations. Details can be referred to our published paper [9]. The flow chart of current solver with sum-rule terms and QUAMBOs is shown in Figure 3.1. The initial step is the preparation for one- and two-electron integrals, that is, the matrix element of Hamiltonian in terms of basis sets. Then the QUAMBOs and the corresponding Hamiltonian matrix are constructed, and the sum-rule terms are added into the system. If the self-consistent calculations does not yield minimum energy, then we determine to further optimize the QUAMBOs until obtain the ground-state energy.

3.7 Results and discussions

Through the examination of analytical solutions in hydrogen dimer case, we have adopted a square root form of the renormalization factor and also added sum-rule terms to the Hamiltonian in order to reduce the errors introduced by the approximations in the CMR method. In this section are presented a series of numerical results generated by the CMR method. Firstly, we performed calculations on hydrogen systems in minimal basis set. Here, hydrogen atoms form one-, two- and three-dimensional structures, showing different bonding environments. Secondly we report the practicability of using QUAMBOs in the CMR method. Thirdly, we further apply the QUAMBO-based CMR

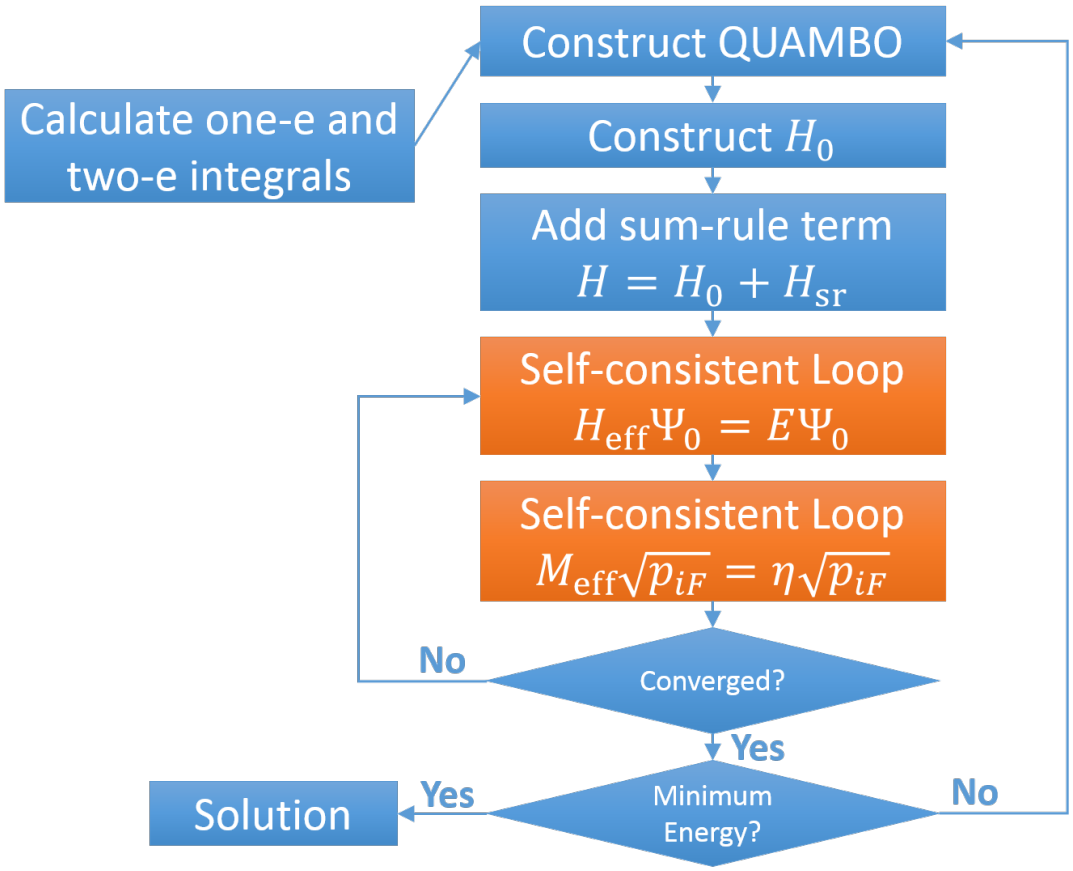

Figure 3.1: Flow chart of the CMR program with sum-rule terms through the approach of QUAMBO. The orange boxes are also self-consistent loops inside for solving the single-particle equations and local configurations.

method in more challenging molecular systems with multi-active orbitals, including N_2, F_2, HF, CO, NH_3 and CH_4.

3.7.1 Hydrogen clusters

The CMR method was performed on multiple hydrogen clusters with STO-3G minimal basis-set orbitals [22], including H_2, H_6 ring, H_6 prism, H_8 ring, H_8 gird, and H_8 cube. The energy calculations of these hydrogen clusters cover one-, two- and three-dimensional structures. The results are presented in the following figures (Figure 3.2, 3.3, 3.4, 3.5, 3.6, and 3.7), showing the potential energy curves and local onsite double occupancies as a function of bond length. Calculations from multiple quantum methods

are included. The results from FCI calculations are exact solutions. In the H_2 case, FCI and the CMR method produce indeed identical results for both the ground state energies and double occupancies, which is as expected based on our analytical discussions. In other systems with different bonding environments, the CMR approach also produces close results compared with FCI.

Note that the local onsite double occupancy presented by FCI is gradually suppressed as the bond length increases. The double occupancy has significant importance in indicating the strength of correlation, while this quantity is fixed at 0.25 for LDA and HF methods. From Eq. 3.41, we can see that the onsite contribution to total energy is proportional to the double occupancy, which is why HF and LDA results show significant deviations from FCI result especially at large atomic separations.

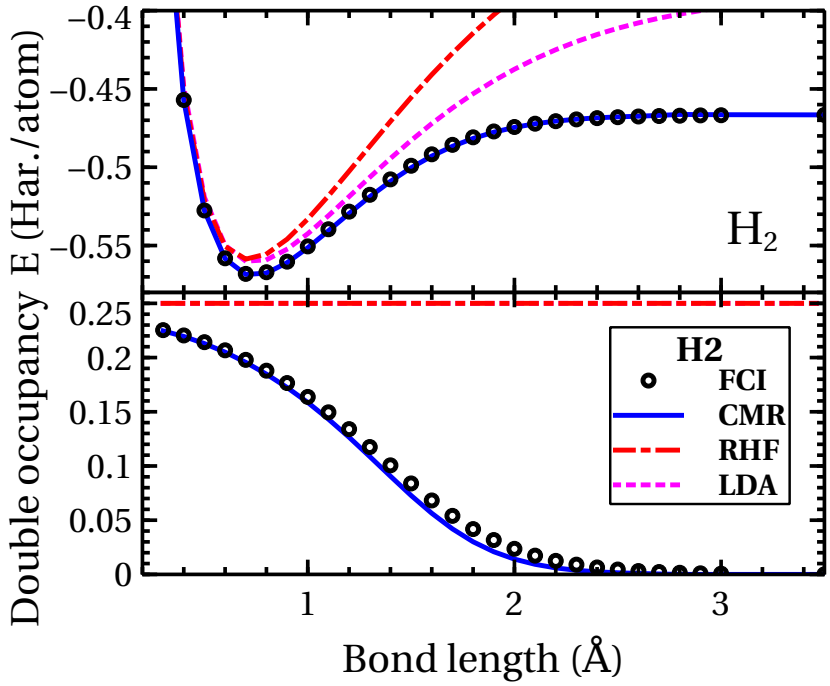

Figure 3.2: Potential energy curve and double occupancy behavior of hydrogen dimer. The upper plot shows potential energy curves. The lower plot shows the corresponding double occupancies as a function of bond length.

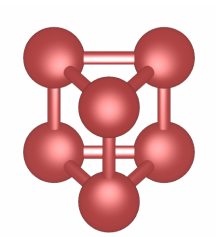

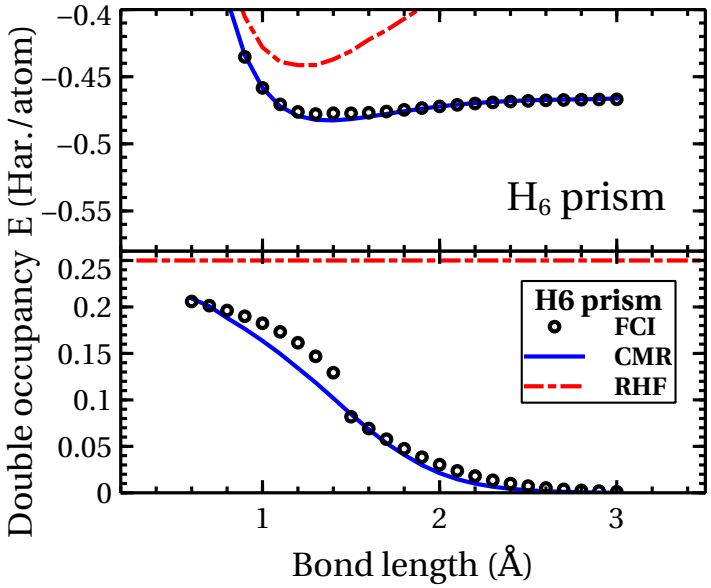

Figure 3.3: Potential energy curve and double occupancy behavior of H_6 prism. The upper plot shows potential energy curves. The lower plot shows the corresponding double occupancies as a function of bond length.

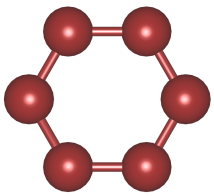

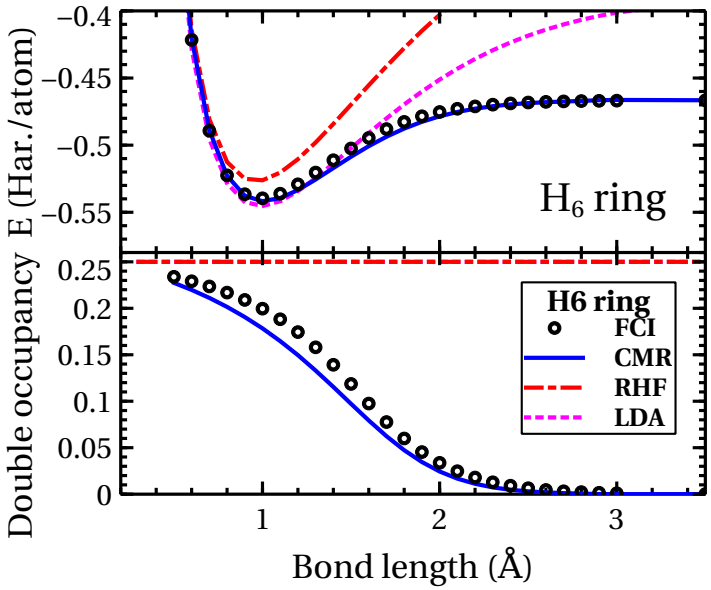

Figure 3.4: Potential energy curve and double occupancy behavior of H_6 ring. The upper plot shows potential energy curves. The lower plot shows the corresponding double occupancies as a function of bond length.

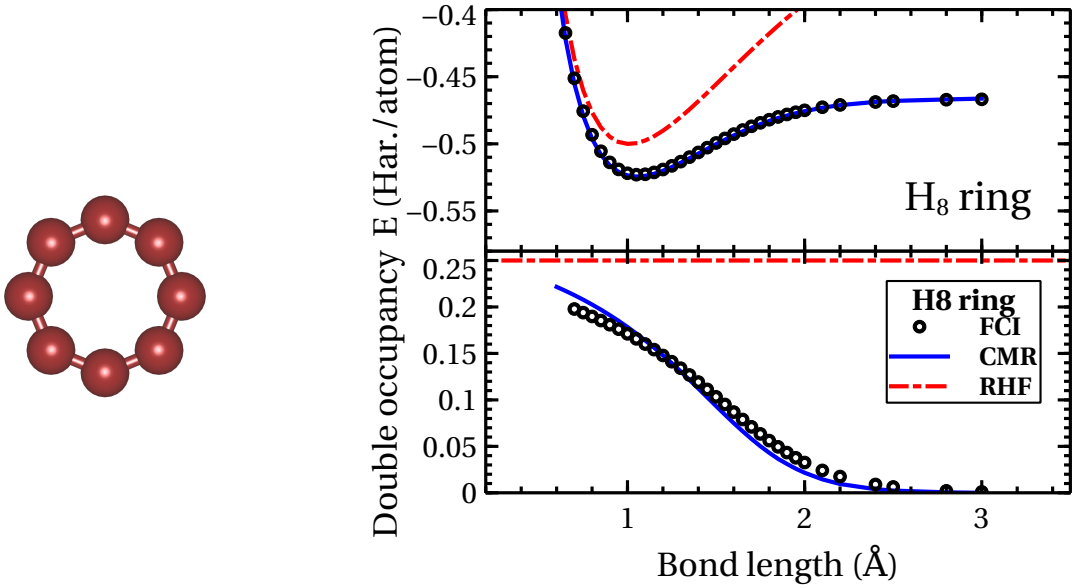

Figure 3.5: Potential energy curve and double occupancy behavior of H_8 ring. The upper plot shows potential energy curves. The lower plot shows the corresponding double occupancies as a function of bond length.

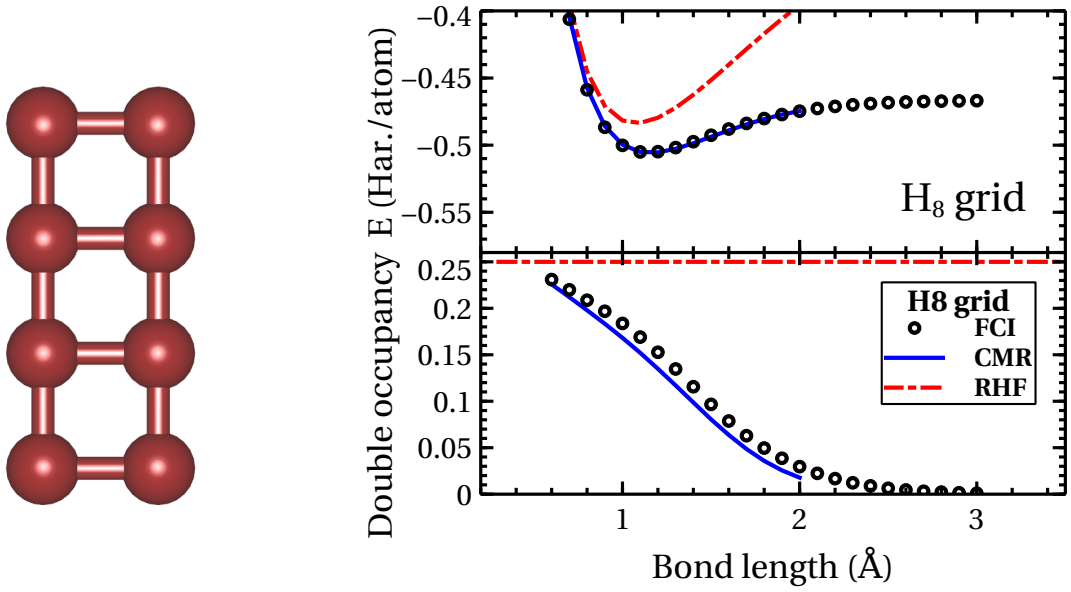

Figure 3.6: Potential energy curve and double occupancy behavior of H_8 grid. The upper plot shows potential energy curves. The lower plot shows the corresponding double occupancies as a function of bond length.

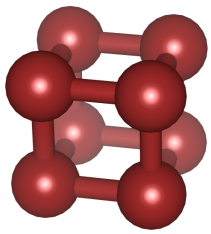

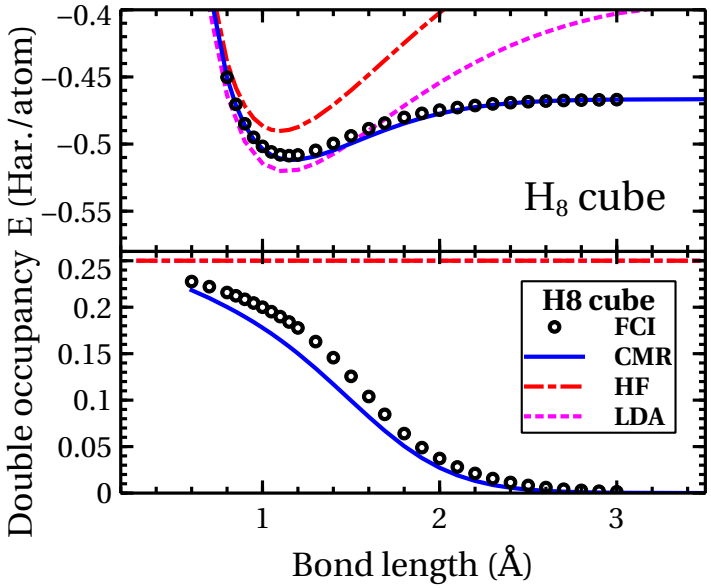

Figure 3.7: Potential energy curve and double occupancy behavior of H_8 cube. The upper plot shows potential energy curves. The lower plot shows the corresponding double occupancies as a function of bond length.

3.7.2 Large basis through QUAMBO approach

It is convenient to study the performance, calculate the energies and examine the theory from simple systems, like the hydrogen clusters with minimal basis set. However, it is the system with large basis sets that allows us to make quantitative predictions and to compare the calculations with experiments. To efficiently construct the GWF from large basis-set orbitals in the CMR method, we utilize the QUAMBO approach, which has proven to be an efficient approximation to the multi-configurational SCF orbitals that can recover a large percent of correlation energy [18, 19].

The performance for QUAMBO-based CMR calculation is demonstrated here by testing the H_2 system with 6-311G(p) basis-set [51] (3 s-orbitals and 1 p-orbital for each hydrogen atom). Based on SCF HF calculations, the 1s-QUAMBO is constructed as a linear combination of the large basis set, and the expansion coefficients are further optimized to minimize the ground state total energy in CMR method. Figure 3.8 shows the QUAMBO-based CMR potential energy curve, together with the large-basis FCI

result and QUAMBO-FCI curve. Note that the QUAMBO-CMR agrees well with the QUAMBO-FCI result, and the binding energy of QUAMBO-CMR is about 9 mhartrees higher than that of large-basis FCI.

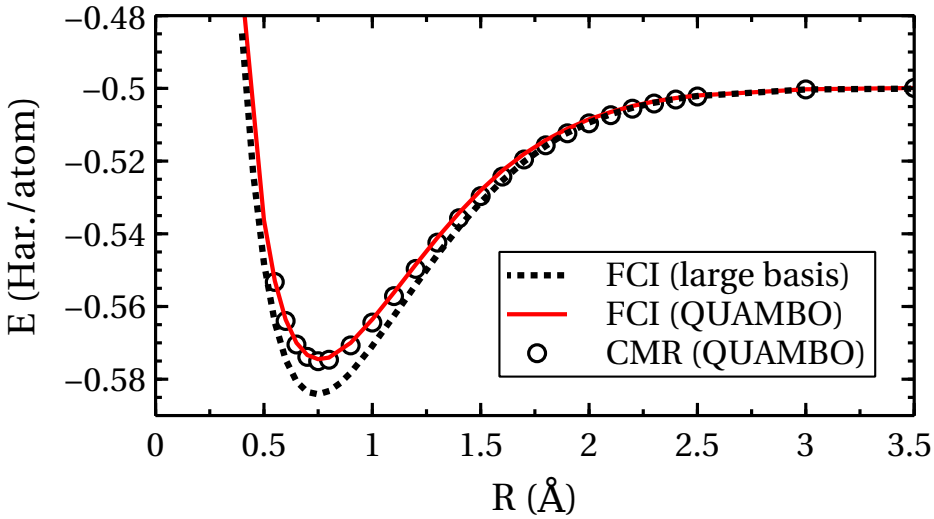

Figure 3.8: Energy curve of H2 calculated by QUAMB-based CMR, as well as QUAMBO-based FCI and large-basis FCI results. The QUAMBOs are constructed from 6-311G(p) basis-set orbitals.

3.7.3 Molecules with multiple active orbitals

We further performed CMR calculations on more challenging systems including homonuclear and heteronuclear molecules. To compare with experiments, we constructed QUAMBOs from aug-cc-pVTZ basis functions, the dunning's correlation consistent basis sets [25]. Three categories of molecules are considered here: homonuclear dimers (N_2 and F_2), heteronuclear dimers (HF and CO), and polyatomic molecules (NH_3 and CH_4), of which the energy curves are shown in Figure 3.9, Figure 3.10 and Figure 3.11. Overall the QUAMBO-CMR results overlap well with the QUAMBO-FCI calculations, and the both curves show good agreement with experimental data. The difference between binding energies of QUAMBO-CMR and experiments is about 11 mhartrees in average for all the molecules considered here, which is summarized in the Table 3.1. The equilibrium

bond lengths produced by QUAMB-CMR also yield close values to the experimental data, since the standard deviation is 0.024 $\AA$. Note that the dissociation curve of N_2 is a challenge in that the nitrogen atom is highly open-shell with three unpaired electrons. The energy curve of F_2 has also proven to be difficult to obtain accurate results fully by *ab initio* calculations [52].

Table 3.1: Summary of equilibrium bond length R_e and binding energy E_b for a series of molecules. QUAMBO-FCI, QUAMBO-CMR and experimental data [1, 2] are included.

	R_e ($\AA$)			E_b (Har./atom)		
	FCI	CMR	Exp.	FCI	CMR	Exp.
H_2	0.744	0.744	0.741	0.073	0.076	0.082
N_2	1.100	1.118	1.098	0.164	0.160	0.180
F_2	1.467	1.467	1.412	0.022	0.030	0.030
CO	1.133	1.121	1.128	0.192	0.186	0.204
HF	0.909	0.942	0.917	0.105	0.100	0.108
CH_4	1.115	1.112	1.087	0.126	0.132	0.126
NH_3	1.012	1.033	1.012	0.106	0.110	0.110
σ	0.024	0.027		0.009	0.011	

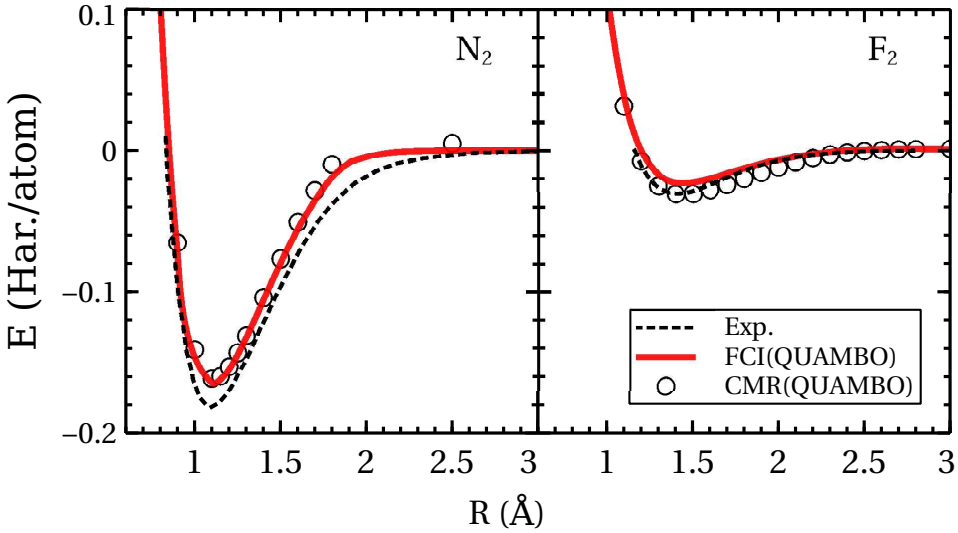

Figure 3.9: Potential energy curves of N_2 and F_2. Included are the CMR and FCI results performed on QUAMBOs constructed from aug-cc-pVTZ basis set. Available experimental data [3, 4] are also included.

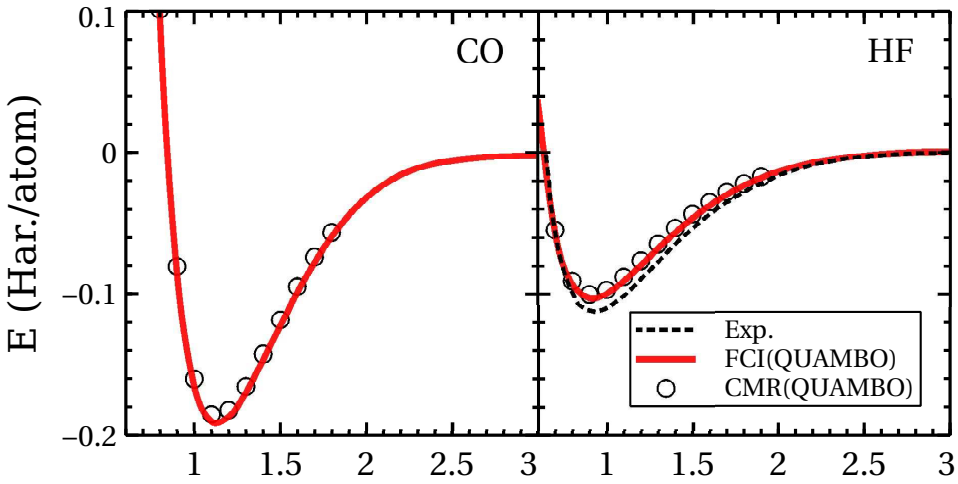

Figure 3.10: Potential energy curves of CO and HF. Included are the CMR and FCI results performed on QUAMBOs constructed from aug-cc-pVTZ basis set. Available experimental data [5] are also included.

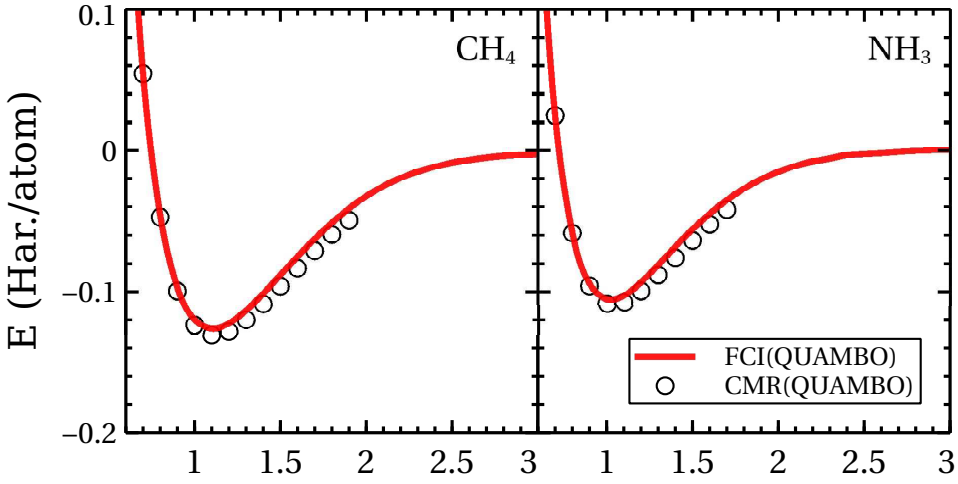

Figure 3.11: Potential energy curves of NH_3 and CH_4. Included are the CMR and FCI results performed on QUAMBOs constructed from aug-cc-pVTZ basis set.

CHAPTER 4. COUPLING CONSTANT INTEGRATION METHOD FOR TOTAL ENERGY CALCULATION

4.1 Introduction

Nowadays density functional theory based on Kohn-Sham approach (KS-DFT) [7] has provided an elegant framework for electronic structure and total energy calculations. KS-DFT provides highly accurate descriptions of the ground state properties of many materials, but it fails in part or completely for systems with significant electron correlation effects. For instance, KS-DFT often gives very poor estimations of the magnetic anisotropic energy (MAE), which is related with the coercivity—a crucial parameter for the applications of ferromagnetic materials.

In the framework of KS-DFT, great efforts have been made for the magnetic anisotropy calculation based on local spin-density approximation (LSDA) [8], as well as the LDA+U method [35, 36]. However, the total energy calculation with spin-orbit coupling (SOC) added requires large amount of computational time with the pursuit of high accuracy. The calculation of magnetic anisotropy usually demands a denser k-point mesh and strict convergence criteria because the scale of MAE is much smaller compared to the total energy. The dynamical mean-field theory (DMFT) [12] has also been extensively used to study the strongly correlated electron systems, but the implementations of DMFT are computationally intensive for systems with SOC. Being one of the many-body theory based methods, the GW method [53] has also been successfully applied to the condensed matter physics. However, one-shot GW method, as well as the quasi-particle

self-consistent GW method [54, 55], is not conserving and difficult to calculate the total energy in systems with SOC.

The magnetic anisotropy, as one of the most important properties of magnetic materials, has drawn considerable attentions in fundamental and technical researches over the years. Materials with the magnetic anisotropy also have attracted industrial interests as promising materials for manufacturing permanent magnets, information storage media or magnetic recording heads. Therefore, there is a need for accurate and time-effective approach to calculate the MAE using electronic structure methods, and also it is necessary to have a better understanding the microscopic origin of the MAE.

In this work, a scheme based on the coupling constant integration (CCI) is applied for magnetic anisotropy calculations in the frame work of DFT. The CCI method [56–59] has provided a lot of insights in the field of DFT, especially in the construction of density functionals for many-body systems. It is known that when the effect of SOC is considered, there would be a small change for the total energies. Through the CCI approach, this change can be computed directly from SOC energies, not from the traditional self-consistent calculations (SCC), which is especially advantageous when the calculations for spin-orbit coupling interaction are less demanding than the total energies. In addition, the MAE, the difference of total energies, can then be expressed by the integration over the difference for SOC energies in different directions. From this viewpoint, we can further decompose the SOC energies and orbital moments dependent on spin and atomic sites, in order to elucidate the origins of MAE.

The following sections begin with an introduction to MAE. Then we presented the formalism and implementation to the CCI method for total energy calculations as well as MAE calculations. Later we performed the CCI method on three non-magnetic bulk materials for total energy calculations, which agrees well with the SCC results. In addition, we also present results for MAE calculations for ferromagnetic materials, CoPt and FePt. Furthermore, we discuss the contributions to MAE in terms of spin and

atomic sites. Though we performed our simulations by DFT within LDA, this integration method is a general approach for total energy calculations with SOC, and it is independent of electronic structure methods.

4.2 Magnetic anisotropy energy

Permanent magnets play an important role in today's industry and technology, ranging from generators and motors to information storage and processing devices. Such wide applications result from the MAE property, which describes the tendency of the magnetization along specific axes. The most preferred axis in ferromagnetic materials is called the easy axis, in contrast to the least preferred axis that is called the hard axis. Materials with high MAE usually have high coercivity, which describes the stability of the magnetization in bulk systems as well as thin films. Extensive research focuses on the search for permanent magnets with higher MAE, and also on the microscopic origins of MAE.

The sources can be divided into the extrinsic and the intrinsic. The extrinsic modifications of the shape, thickness, and stress can tune the MAE, especially in the case of thin films. The intrinsic origin of MAE should not result from the exchange interaction between spins, due to the invariance for a rotation of the magnetization direction. The true origin should be linked to the crystal symmetry and atomic composition. One proposed explanation is the classical magnetic dipole-dipole interaction between spins, but calculations show that the contribution is several orders smaller than experimental results [60]. In most cases, there should be more dominant sources of anisotropy. The SOC, the interaction between the spin of electron and orbital magnetization, was proposed by Van Vleck [61] to contribute to the anisotropy energy. This statement is generally valid, but it is still not clear that what kind microscopic mechanisms are responsible for the origins and variations of the MAE.

One way to calculate MAE is using *ab initio* electronic structure methods with DFT, in which the spin-orbit term needs be incorporated. The SOC is one of the relativistic effects. In the full potential relativistic linearized augmented plane-wave (LAPW) [62] method that is used in our work, the relativistic effects are implemented in different levels. As we have mentioned in previous chapters, the space in a unit cell is divided into the muffin-tin and interstitial regions. There is no implementation of relativistic effect in interstitial regions, in that the SOC is considered as a localized interaction that is large in the neighborhood around nucleus. In the muffin-tin region, the core states are fully occupied and calculated with spin-compensated Dirac equations that contain the SOC. Therefore, the core electrons are fully relativistic, whereas the valence electrons are treated within a scalar relativistic approximation that is the Dirac equation without SOC term. If the SOC is included in the Dirac equations, the l, s will no longer be good quantum numbers (j and κ instead), and the construction and diagonalization of Hamiltonian are time-consuming. Rather the SOC can be added in second variational treatment of wavefunctions. The comparison is illustrated in the diagram shown in Figure 4.1.

4.3 Formulation

4.3.1 Total energy and MAE from CCI

The total Hamiltonian with SOC term is usually written as,

$$\mathcal{H} = \mathcal{H}_0 + \xi \boldsymbol{L} \cdot \boldsymbol{S}, \tag{4.1}$$

where $\mathcal{H}_0$ is the Hamiltonian with scalar relativistic effects, and $\xi \boldsymbol{L} \cdot \boldsymbol{S}$ denotes the SOC Hamiltonian. We now define a coupling-constant-dependent Hamiltonian by adding a coupling constant λ for SOC term,

$$\mathcal{H} = \mathcal{H}_0 + \lambda V, \tag{4.2}$$

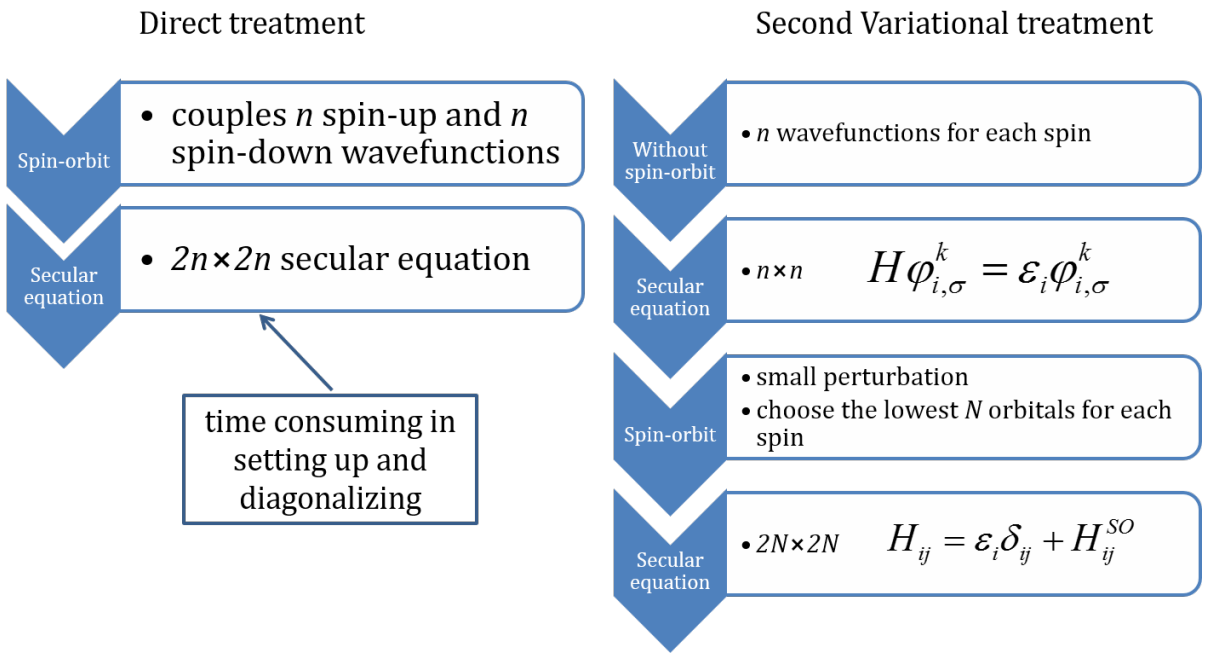

Figure 4.1: Comparison of direct treatment and second variational treatment for spin-orbit effects. The left plot shows the direct treatment including SOC in Dirac equations, which requires setting up and diagonalizing a large matrix. The right plot shows the second variational treatment, in which the SOC is treated as the perturbation only for lowest-lying orbitals.

where $V = \xi \boldsymbol{L} \cdot \boldsymbol{S}$. The expectation value of total energy is given by,

$$E(\lambda) = \langle \Psi(\lambda) | \mathcal{H} | \Psi(\lambda) \rangle . \tag{4.3}$$

Especially, $E(\lambda = 0)$ denoted as E_{scalar} is the total energy with scalar relativistic effects, and $E(\lambda = 1)$ denoted as E_r is the total energy with SOC added. The expectation value of spin-orbit interaction becomes,

$$E^{\text{so}}(\lambda) = \langle \Psi(\lambda) | \lambda V | \Psi(\lambda) \rangle . \tag{4.4}$$

According to the Hellmann-Feynman theorem, we can express the derivative of total energy in terms of λ as,

$$\begin{aligned} E'(\lambda) &= \frac{\partial E}{\partial \lambda} \\ &= \langle \Psi(\lambda) | \frac{\partial(\mathcal{H}_0 + \lambda V)}{\partial \lambda} | \Psi(\lambda) \rangle \\ &= \langle \Psi(\lambda) | V | \Psi(\lambda) \rangle \\ &= \frac{E^{\mathrm{so}}(\lambda)}{\lambda}. \end{aligned} \tag{4.5}$$

Thus we can calculate the total energy from integration over the coupling constant,

$$E(\lambda) = E_{\mathrm{scalar}} + \int_0^{\lambda} \frac{E^{\mathrm{SO}}(\lambda')}{\lambda'} d\lambda', \tag{4.6}$$

and also,

$$E_r = E_{\mathrm{scalar}} + \int_0^{1} \frac{E^{\mathrm{SO}}(\lambda')}{\lambda'} d\lambda'. \tag{4.7}$$

Put differently, when SOC is added to the scalar-relativistic Hamiltonian, the induced energy change can be expressed by the integration over SOC energies divided by the coupling constant. Finally, we can find the MAE, the difference in energies for two different magnetization directions (e.g., [100] and [001]), to be expressed by,

$$\mathrm{MAE} = \int_0^{1} \frac{E^{\mathrm{SO}}_{100}(\lambda) - E^{\mathrm{SO}}_{001}(\lambda)}{\lambda} d\lambda \tag{4.8}$$

4.3.2 Decomposition of SOC energy

In order to obtain an understanding of the microscopic origin of MAE, we can decompose the spin-orbit coupling energy to different spin components. We have known that the ensemble average for an operator $\mathbf{A}$ can be written as the trace of the product of density matrix ρ and $\mathbf{A}$ in terms of a basis set $\{i\}$,

$$\begin{aligned} \langle \mathbf{A} \rangle &= Tr(\rho \mathbf{A}) \\ &= \sum_i \sum_{i'} \langle i | \rho | i' \rangle \langle i' | \mathbf{A} | i \rangle. \end{aligned} \tag{4.9}$$

Considering collinear spin systems, the basis $\{i\}$ can be split into two sets, $\{\alpha\}$ with spin-up wavefunctions and $\{\beta\}$ with spin-down wavefunctions, giving the expectation of $\mathbf{A}$ as,

$$\begin{aligned}\langle \mathbf{A} \rangle = &\sum_{\alpha} \langle \alpha|\rho|\alpha\rangle\langle\alpha|\mathbf{A}|\alpha\rangle \\ &+ \sum_{\alpha\beta} \langle \beta|\rho|\alpha\rangle\langle\alpha|\mathbf{A}|\beta\rangle \\ &+ \sum_{\alpha\beta} \langle \alpha|\rho|\beta\rangle\langle\beta|\mathbf{A}|\alpha\rangle \\ &+ \sum_{\beta} \langle \beta|\rho|\beta\rangle\langle\beta|\mathbf{A}|\beta\rangle\end{aligned} \tag{4.10}$$

Based on the decomposition, we can study the contributions of the atomic site and spin-transition process to the spin-orbit interactions, as well as the MAE.

4.4 Results and discussions

4.4.1 Total energy from CCI

To confirm the validity of the CCI given in Eq. 4.6, we carried out all-electron first-principle density-functional calculations using the full potential relativistic linearized augmented plane-wave (LAPW) [62] package (Wien2K) [63]. Three single-element face-centered cubic (FCC) crystals Al, Pt and Pu, which have increasing spin-orbit interactions, are of our interest. Through our calculations, the values we used as lattice constants are, $7.653a.u.$, $7.417a.u.$ and $8.754a.u.$. The self-consistent calculations are done with a $21 \times 21 \times 21$ k-point mesh using LSDA as the exchange-correlation functional, and the temperature broadening method is used for summation over k-points in the first Brillouin zone corresponding to the unit cell of FCC structure.

When the SOC is considered, we want to compare the CCI with SCC for the change in total energies at different coupling strength. For multiple values of λ, we can calculate the change in total energies from integration over $E^{\mathrm{SO}}(\lambda)/\lambda$ through the CCI approach.

The energy change can also be acquired from the SCC. These two methods are compared in Fig. 4.2, in which the curve calculated from CCI exactly goes through all the data points from SCC. To simplify the discussion, we exclude the energy with scalar relativistic effects from total energies for clarity and focus on the change of the total energies when SOC is considered.

At $\lambda = 1$, numerical values for thorough comparisons are given in Table 4.1. The relative errors are smaller than half percent, indicating that the CCI method is a good approach to the total energy calculations.

Table 4.1: Comparison of the total energy change, calculated from the CCI and from the SCC.

	Al	Pt	Pu
E_{SCC}/meV	-0.57253	-1211.84	-2591.67
E_{CCI}/meV	-0.57244	-1208.57	-2594.06
Error (%)	0.016	0.270	0.092

4.4.2 MAE from CCI

With Eq. 4.8, we can further apply the CCI method to compute MAE of realistic systems, by means of relativistic band-structure calculations within LSDA. Two typical examples of ferromagnetic materials with high MAE are FePt and CoPt that both have the $L1_0$ structure. We took experimental values as lattice constants: $a = 5.218a.u$, $c = 7.058a.u.$ for FePt and $a = 5.070a.u.$, $c = 6.97a.u.$ for CoPt [64]. The MAE we calculated amounts to the difference for two magnetization orientations [100] and [001] ([001] axis is set perpendicular to the alternating Fe/Co and Pt planes and the second nearest in-plane neighbor lies on the [100] axis.). In order to reduce the numerical errors, we use the same symmetry group for two orientations, and so is the k-point mesh being set to $40 \times 40 \times 29$. Even though FePt and CoPt both exhibit large MAE compared to other materials, the scale is still just around meV, much smaller than total energy. Hence the tiny energy scale in MAE calculation is a serious challenge for numerical methods.

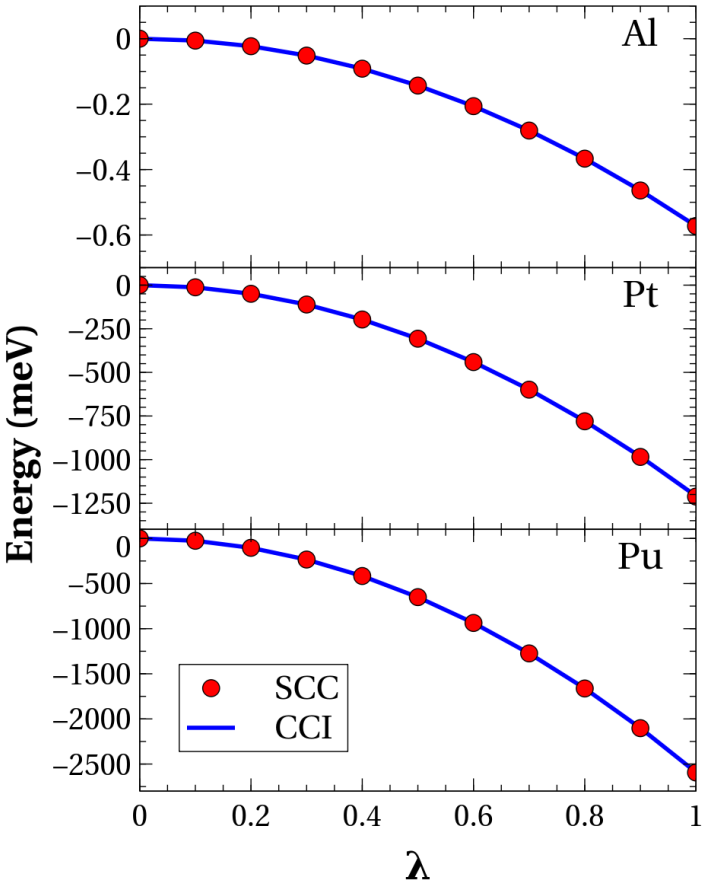

Figure 4.2: Comparison of two methods for the total energy change in terms of λ for FCC crystals Al(top), Pt(middle) and Pu(bottom). Energies from SCC at different λs are indicated as red solid circles, and the solid curves are calculated from CCI.

However, the results from the CCI method still show impressive agreement with those from SCC in Fig. 4.3. Our calculations for MAE also present a reasonable agreement with previous studies [65–67].

In order to further study the efficiency and accuracy of the CCI method, we varied the number of data points for integration. The results are presented in Table 4.2. Ten points integration is constructed by data from 0.0 to 1.0 incremented by 0.1. Five data points integration are from 0.0 to 1.0 incremented by 0.2, and three points integration chooses data at 0.0, 0.5 and 1.0. The errors are consistently relative small even for less number of data points.

Table 4.2: Comparison of the MAE per formula unit for FePt and CoPt calculated from two methods. The MAE with its relative errors from the CCI method is also listed according to three different numbers of data points.

	FePt	CoPt
E_{SCC}/meV	2.505	1.269
E_{CCI}/meV (Error)		
3 points	2.426 (3.1%)	1.264 (0.4%)
5 points	2.429 (3.0%)	1.258 (0.9%)
10 points	2.474 (1.2%)	1.257 (0.9%)

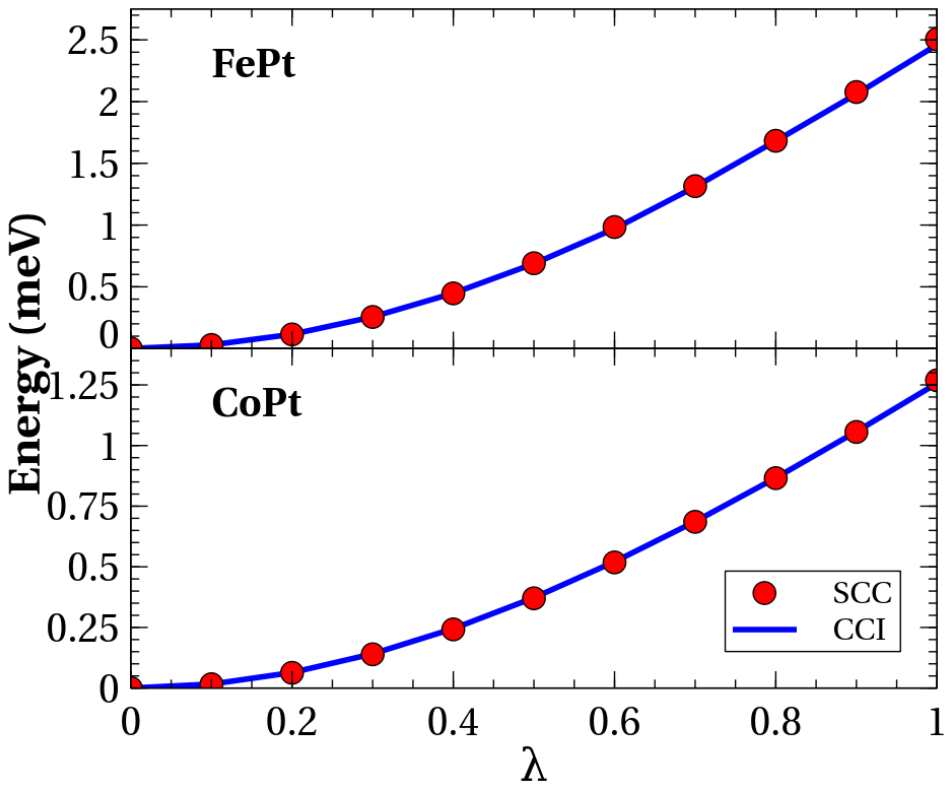

Figure 4.3: Comparison of two methods for magnetic anisotropy energy calculations for FePt and CoPt at different values of λ. Red dots indicate the MAE calculated from self-consistent calculations, while the solid line is the MAE acquired from integration over the coupling constant.

4.4.3 Decomposition of E^{SO}

Table 4.3: Decomposition of spin-orbit coupling energy E_{SO}(meV) and orbital magnetic moment $M_l(m\mu_B)$ into different atomic sites and spin components. The anisotropies of E_{SO} and M_l for two different orientations are defined as $K_{SO} = E^x_{SO} - E^z_{SO}$ and $K_l = M^z_l - M^x_l$.

FePt		Pt					Fe				
		↑↑	↑↓	↓↑	↓↓	Total	↑↑	↑↓	↓↑	↓↓	Total
	z	-393.1	-806.1	-806.1	-404.2	-2409.5	-4.5	-9.1	-9.1	-6.1	-28.8
E_{SO}	x	-389.8	-804.3	-804.3	-405.5	-2403.9	-4.9	-9.6	-9.6	-6.2	-30.3
	K_{SO}	3.3	1.8	1.8	-1.3	5.6	-0.4	-0.5	-0.5	-0.1	-1.5
	z	-173			222	49	-16			79	63
M_l	x	-160			220	60	-25			83	58
	K_l	-13			2	-11	9			-4	5
CoPt		Pt					Co				
		↑↑	↑↓	↓↑	↓↓	Total	↑↑	↑↓	↓↑	↓↓	Total
	z	-393.1	-809.9	-809.9	-407.2	-2420.1	-5.5	-10.7	-10.7	-8.7	-35.6
E_{SO}	x	-389.1	-809.1	-809.1	-409.7	-2417.0	-6.0	-11.4	-11.4	-7.8	-36.6
	K_{SO}	4.0	0.8	0.8	-2.5	3.1	-0.5	-0.7	-0.7	0.9	-1.0
	z	-172			229	57	-21			109	88
M_l	x	-160			234	74	-30			85	55
	K_l	-12			-5	-17	9			24	33

According to Bruno's relation [68], the MAE is proportional to the anisotropy of the orbital magnetic moment, but the previous study [69] on FePt and CoPt shows that the easy axis does not coincide with the direction with the largest orbital magnetic

moment. Calculated by the LAPW package WIEN2K, results in Table 4.3 show the decomposition of SOC energies and orbital magnetic moment into different atomic sites and spin-transition processes for FePt and CoPt. We found that the Pt site makes a considerable and positive contribution to the MAE, while Fe/Co site makes a smaller negative contribution. Furthermore, the anisotropy of spin-conservation terms in Pt site, especially the term for the majority spin channel, makes larger contribution compared to spin-flip terms, which is more obvious in CoPt. These discussions are in agreement with previous work [67] through perturbation theory using the Vienna ab initio simulation package.

CHAPTER 5. INVESTIGATION OF GROUND STATE TRANSITION IN $CaIrO_3$ BY DFT+DMFT

5.1 Introduction

The discovery of cuprate superconductors has aroused wide interests in electron correlation effects in transition metal compounds, which has been one of the most important areas in condensed matter physics. Many of these compounds exhibit metal-insulator transitions (MIT). In $3d$ transition metal compounds, the MIT is classified as Mott transition that is driven by on-site Coulomb repulsion, due to the localized $3d$ orbitals. However, the electron correlation effects that are significant in $3d$ transition metal compounds become weaker in $4d$ and $5d$ transition-metal oxides since the orbitals of valance electrons are more delocalized. On the other hand, the spin-orbit interaction increases for heavier elements, and the strength can be comparable with correlation effects of $5d$ electron systems. Therefore, intriguing physics is expected to observe for $5d$ transition metal compounds due to the interplay between the spin-orbit interaction, electron correlation, inter-site hopping, and crystal-field splitting.

One of the most representative $5d$ model system is Iridium oxides, including Sr_2IrO_4 [70–72], Ba_2IrO_4 [73] and $CaIrO_3$ [74, 75]. In our work, we investigated the electronic structure of the postperovskit $CaIrO_3$, of which the nature of ground state is in debate [74, 75]. The MIT in $CaIrO_3$ is accompanied by the emergence of antiferromagnetic (AFM) order, in contrast to conventional Mott insulators. Even though various magnetic transitions are very common in tradition Mott insulators, the transition itself is

not correlated with any magnetic transition, but the insulating ground state in $CaIrO_3$ appears only when the AFM order emerges. Thus they are supposed to be classified into Slater insulators instead of Mott insulators.

We need reliable tools to study the electronic structure of these $5d$ electron systems. The Kohn-Sham density functional theory (KS-DFT) is unable to describe strongly correlated systems, in that the approximations to the unknown exchange-correlation functional from non-interacting systems cannot fully capture the strong interactions. A powerful theory successful in studying these materials is the dynamical mean-field theory (DMFT) [12–14], in which the model many-body Hamiltonian is mapped on a quantum impurity model self-consistently. Only a small number of degree of freedoms needs to be solved in the quantum impurity model, in which the interacting system is immersed in a bath of non-interacting system. The DMFT requires to start from a model Hamiltonian, which can be constructed from the traditional DFT calculations for realistic materials. Therefore, we employed the DMFT problem on top of DFT computation, and demonstrated that the gap formation in $CaIrO_3$ is resulting from Slater mechanism.

5.2 A combination of the DFT and DMFT

Correlation effects can be understood as the effects beyond factorization approximations, that is, the expectation value of the product of two correlated operators is not equal to the product of the two corresponding expectation values. Mathematically, it can be expressed by:

$$\langle \hat{O}_i \hat{O}_j \rangle \neq \langle \hat{O}_i \rangle \langle \hat{O}_j \rangle. \tag{5.1}$$

A mean-field theory aims to approximate the whole problem by an effective single-site (single spin) problem. A simple illustration is the Weiss mean field theory in Ising model with ferromagnetic coupling, which is given by,

$$\mathcal{H} = -\sum_{ij} J_{ij} S_i S_j - h \sum_i S_i. \tag{5.2}$$

For the effective Hamiltonian at a given site i, all the degree of freedoms from other sites can be approximated by an effective field h_{eff}:

$$\mathcal{H}_{i,\text{eff}} = -h_{\text{eff}} S_i \tag{5.3}$$

where

$$h_{\text{eff}} = h + \sum_j J_{ij} \langle S_i \rangle. \tag{5.4}$$

Given the coordination number z, $J = J_{ij}$, and $\langle S \rangle \equiv \langle S_i \rangle$, this yields the mean-field equation:

$$\langle S \rangle = \tanh\Big(\beta h + z\beta J \langle S \rangle\Big) \tag{5.5}$$

where $\beta \equiv 1/(k_B T)$. This equation is the true solution of the Ising model when z goes large, and the coupling J need be rescaled as J^*/z.

The mean-field idea can be extended to Hubbard model as well:

$$H = -t_{ij} \sum_{\langle i,j \rangle, \sigma} c^\dagger_{i\sigma} c_{j\sigma} + U \sum_i n_{i\uparrow} n_{i\downarrow} \tag{5.6}$$

where t_{ij} is the electron hopping energy from site i to site j, and U is the on-site Coulomb repulsion energy. The mean-field idea can be implemented through a single-site ("impurity") action:

$$\begin{aligned} S_{\text{eff}} = &- \int_0^\beta d\tau \int_0^\beta d\tau' \sum_\sigma c^\dagger_{o\sigma}(\tau) \mathscr{G}_0^{-1}(\tau - \tau') c_{o\sigma}(\tau') \\ &+ U \int_0^\beta d\tau \, n_{o\uparrow}(\tau) n_{o\downarrow}(\tau) \end{aligned} \tag{5.7}$$

where the operators with symbol o indicate that they are at site o. $\mathscr{G}_0^{-1}(\tau - \tau')$ is the inverse effective local propagator or bath Green function, which plays the role like the effective field in Weiss mean-field theory. The physical meaning is an effective amplitude for an electron to be created on the site o at time τ and destroyed at time τ'. The effective action can yield local Green function [12], written as $G(\mathrm{i}\omega) = \int_0^\beta d\tau G(\tau) e^{\mathrm{i}\omega_n \tau}$ where $w_n \equiv (2n+1)\pi/\beta$ and

$$G(\tau - \tau') \equiv -\langle T c(\tau) c^\dagger(\tau') \rangle_{S_{\text{eff}}}. \tag{5.8}$$

On the other hand, Dyson equations can also produce the lattice Green function in terms of self-energy:

$$\begin{aligned} G(\mathrm{i}\omega) &\equiv G_{ii}(\mathrm{i}\omega) \\ &= \frac{1}{V_B}\sum_k \frac{1}{\omega + E_f - \epsilon_k - \Sigma(\omega)} \\ &= \int_{-\infty}^{\infty} \frac{N^0(\epsilon)}{\omega + E_f - \epsilon_k - \Sigma(\omega)}. \end{aligned} \tag{5.9}$$

It can be shown that the lattice Green function is equal to the local Green function [12].

The effective on-site problem will in turn yield the self-energy, given by

$$\Sigma(\mathrm{i}\omega_n) = \mathscr{G}_0^{-1}(\mathrm{i}\omega_n) - G^{-1}(\mathrm{i}\omega_n). \tag{5.10}$$

The Eq. 5.7, Eq. 5.8, Eq. 5.9 and Eq. 5.10 form a self-consistency cycle in DMFT implementations demonstrated in Figure 5.1 [76].

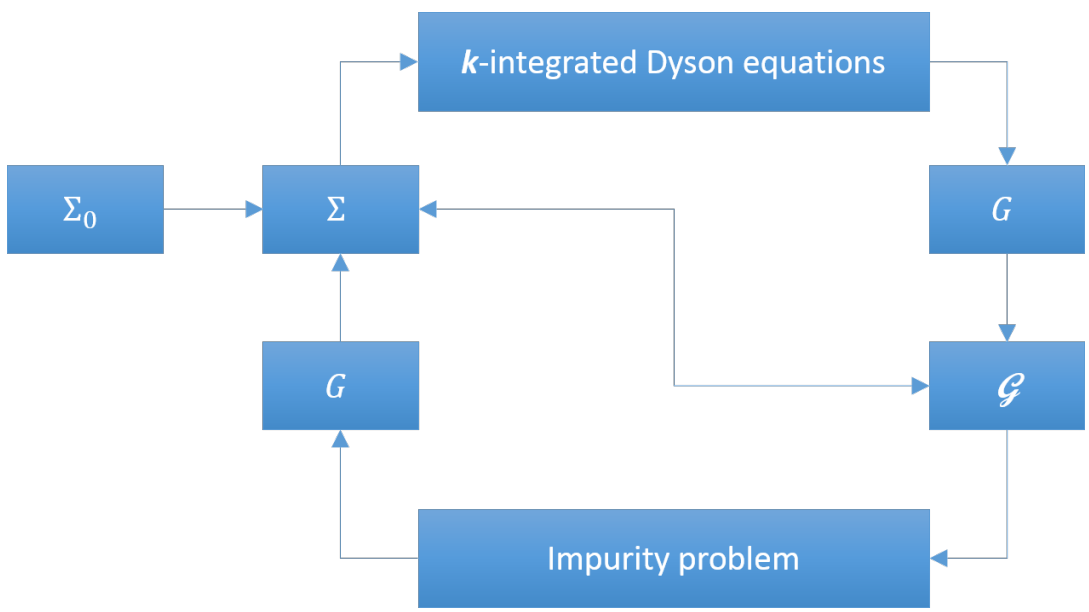

Figure 5.1: The self-consistency cycle in DMFT calculations.

Though the DMFT methods can successfully describe the strongly electron correlation, they are still model Hamiltonian-based, in which the input parameters are unknown. The application of DMFT methods for realistic materials requires the model to be system

specific, that is, the input parameters are determined by the lattice structure and orbital degeneracy that is unique for each compound. One approach is to incorporate the material specific *ab initio* electronic structure calculations. The DFT methods already have a great success for studying weakly correlated materials but not for strongly correlated phenomena, and the code packages are reliable, robust, fast and actively maintained. Hence, the two complementary methods, DFT and DMFT, can be merged together, shown in Figure 5.2 [12, 14].

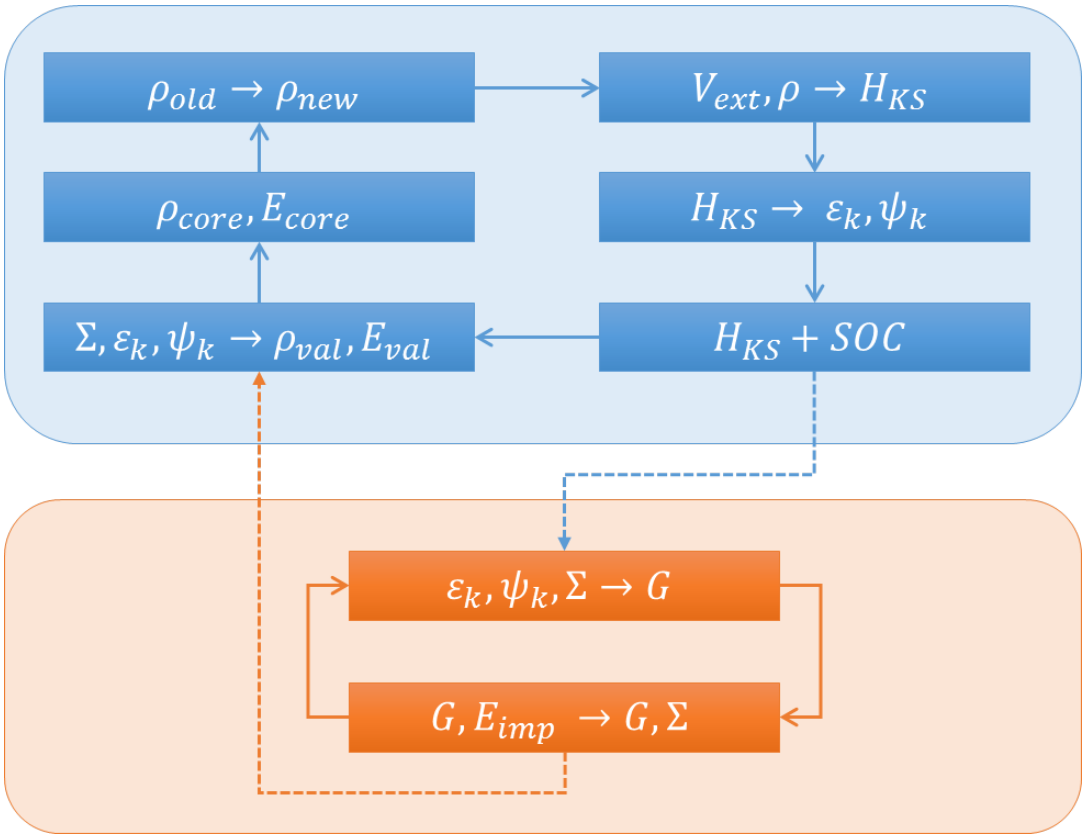

Figure 5.2: The self-consistency cycle in DFT+DMFT calculations.

The whole DFT+DMFT program contains two cycles: the DFT cycle and the DMFT cycle. In DFT cycle, the electronic potential is constructed by initial guess of charge density, and eigenvalue problem is solved for Kohn-Sham orbitals. Next, the spin-orbit coupling is then added as a perturbation and charge densities are mixing for input. After certain number of loops, the DFT part provides the Hamiltonian to the DMFT part,

meanwhile an initial guess of self-energy is also required for the model Hamiltonian. The DMFT cycle uses impurity solver to update the self-energy and charge density iteratively. After certain number of iterations, the DMFT then outputs the band energies to help the DFT part improve the electronic density.

5.3 Computational details of the DFT+DMFT calculation

In $5d$ electron systems, the on-site Coulomb repulsion is much weaker than in $3d$ and $4d$, due to the delocalized valence orbitals. However, the Ir compound, $CaIrO_3$, has an AFM insulating ground state. Such unusual behavior can be elucidated in a scenario of Slater mechanism. The Ir t_{2g} orbital is at first split into completely filled $j_{\text{eff}} = 3/2$ bands, and a half-filled $j_{\text{eff}} = 1/2$ band around the Fermi level due to the spin-orbit coupling (SOC). The latter band is further split into a lower occupied band and an unoccupied one. Here, for clarity, we should use "doublet" and "singlet" notations for these bands, in that the theory of Mott-Hubbard transition also adopts the effective j notation. However, it is more straightforward to present the degeneracy of orbitals using effective j.

Figure 5.3 shows the postperovskit structure of CaIrO3 [20], in which the IrO_6 octahedra share edges along the a axis and share corners along the c axis.

Our DMFT calculations were performed in a fully charge self-consistent way combined with DFT using the projection-embedding implementation [14, 77]. The DFT calculations within the generalized gradient approximation (GGA) [78] were carried out on the full-potential linearized augmented plane-wave (FLAPW) method as implemented in the WIEN2K package [63]. In the DMFT part, we solve the quantum impurity model using the continuous-time quantum Monte Carlo method [79, 80]. The functional [14, 81]

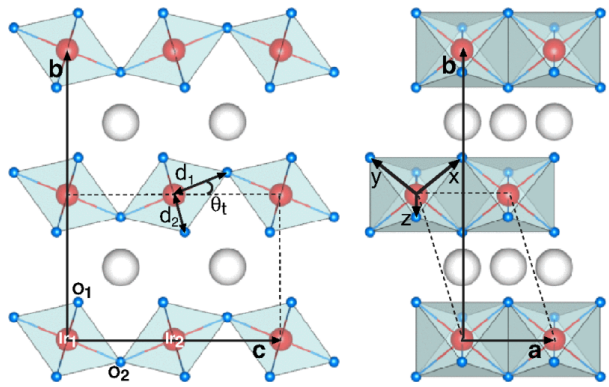

Figure 5.3: The left panel is the postperovskit structure of CaIrO3 projected on the *bc* plane, and the right one is the projection on the *ab* plane. Ca, Ir, and O atoms are represented by circles with large, medium, and small sizes, respectively. The conventional unit cell is indicated by dash lines.

that we want to extremize has the form of,

$$\begin{aligned}\Gamma[\rho, V_{KS}, G_{\rm loc}, \Sigma, V_{dc}, n_d] = &- \mathrm{Tr}\ln\Bigg\{(i\omega + \mu + \nabla^2 - V_{KS})\delta(\mathbf{r}-\mathbf{r}') \\ &- \sum_{\tau LL'} P(\mathbf{r}\mathbf{r}', \tau LL')(\Sigma - V_{dc})_{L'L}\Bigg\} \\ &- \int (V_{KS} - V_{ext})\rho\, d^3r - \mathrm{Tr}(\Sigma G_{loc}) + \mathrm{Tr}(V_{dc} n_d) + \Psi_H[\rho] \\ &+ \Psi_{xc}[\rho] + \Psi_{\rm DMFT}[G_{loc}] - \Psi_{dc}[n_d].\end{aligned} \tag{5.11}$$

The stationarity requires the following derivatives to be zero:

$$\begin{aligned}&\frac{\delta\Gamma}{\delta V_{kS}} = 0 \Rightarrow \\ &\qquad \mathrm{Tr}_\omega\Big(G(\mathbf{r}\mathbf{r}'\delta(\mathbf{r}-\mathbf{r}'))\Big) - \rho(\mathbf{r}) = 0 \\ &\frac{\delta\Gamma}{\delta\rho} = 0 \Rightarrow \\ &\qquad -(V_{KS} - V_{ext}) + \frac{\delta[\Psi_H + \Psi_{xc}]}{\delta\rho} = 0 \\ &\frac{\delta\Gamma}{\delta G_{loc}} = 0 \Rightarrow \\ &\qquad -\Sigma + \frac{\delta\Psi^{\rm DMFT}[G_{loc}]}{\delta G_{\rm loc}} = 0,\end{aligned} \tag{5.12}$$

$$
\begin{aligned}
&\frac{\delta\Gamma}{\delta\Sigma} = 0 \Rightarrow \\
&\qquad \mathrm{Tr}_{\mathbf{r}}\Big(P(\mathbf{r}\mathbf{r}', \tau LL')G\Big) - G_{loc} = 0, \\
&\frac{\delta\Gamma}{\delta V_{dc}} = 0 \Rightarrow \\
&\qquad -\mathrm{Tr}_{\omega\mathbf{r}}\Big(P(\mathbf{r}\mathbf{r}', \tau LL')G\Big) + n_d = 0, \\
&\frac{\delta\Gamma}{\delta n_d} = 0 \Rightarrow \\
&\qquad -V_{dc} - \frac{\delta\Psi_{dc}}{\delta n_d} = 0
\end{aligned}
\tag{5.13}
$$

where $\mathrm{Tr}_\omega = T\sum_{i\omega_n}$ and $\mathrm{Tr}_{\mathbf{r}} = \int d^3r d^3r'$. Here ρ is the electronic charge density, V_{KS} is the Kohn-Sham potential, G_{loc} is the local Green's function, Σ is the self-energy, V_{dc} is the potential of double-counting, n_d is the occupancy of the correlated orbital, $\Psi_H[\rho]$ is the Hartree functional of charge density, $\Psi_{xc}[\rho]$ is the exchange-correlation energy functional, $\Psi_{DMFT}[G_{loc}]$ is the sum of all skeleton diagrams constructed from G_{loc} and Coulomb repulsion U, V_{ext} is the external potential, $P(\mathbf{r}\mathbf{r}', \tau LL')$ is the projector to the local correlated orbital at atom τ with angular momentum L, L'.

The local correlated orbitals are projected from a 20eV energy window around the Fermi level. The double-counting functional is expressed as $\Phi_{dc}(n_d) = n_d E_{dc}$, where $E_{dc} = U(n_d^0 - 1/2) - J/2(n_d^0 - 1)$ and the nominal occupancy n_d^0 of Ir^{4+} ion in $CaIrO_3$ is 5. Due to the large energy window, the local Coulomb interaction parameters are system-independent and estimated [82] as $U \approx 4.5$ eV and $J \approx 0.8$ eV [81]. We set up different local coordinates on each Ir atom in order to simulate the non-collinear antiferromagnetic structure. With the crystal-field and spin-orbit coupling (SOC) interactions considered, the effective $J_{\mathrm{eff}} = 1/2$ states are constructed [81] as,

$$
\begin{aligned}
|\psi_{+\frac{1}{2}}\rangle &= -\sqrt{\frac{3 - 2\gamma(\omega)^2}{3}}|d_{xy}, -\sigma\rangle + \frac{\gamma(\omega)}{\sqrt{3}}(|d_{yz}, +\sigma\rangle - i|d_{xz}, +\sigma\rangle) \\
|\psi_{-\frac{1}{2}}\rangle &= +\sqrt{\frac{3 - 2\gamma(\omega)^2}{3}}|d_{xy}, +\sigma\rangle + \frac{\gamma(\omega)}{\sqrt{3}}(|d_{yz}, -\sigma\rangle + i|d_{xz}, -\sigma\rangle)
\end{aligned}
\tag{5.14}
$$

where σ describes the spin. The value of γ at low-frequency limit is adopted in our transformation in which $\gamma(\omega = 0) \approx 1.2$, since it is more related to spin dynamics. The expectation value of orbital and spin moments under the subspace of $|\psi_{\pm 1/2}\rangle$ can thus be evaluated by,

$$\langle \hat{L} \rangle = \begin{bmatrix} \langle \psi_{+\frac{1}{2}} | \hat{L} | \psi_{+\frac{1}{2}} \rangle & \langle \psi_{+\frac{1}{2}} | \hat{L} | \psi_{-\frac{1}{2}} \rangle \\ \langle \psi_{-\frac{1}{2}} | \hat{L} | \psi_{+\frac{1}{2}} \rangle & \langle \psi_{-\frac{1}{2}} | \hat{L} | \psi_{-\frac{1}{2}} \rangle \end{bmatrix} \tag{5.15}$$

where $\hat{L}$ can be the orbital or spin moment operator. The magnitudes of magnetic moments along the magnetization axis can be calculated as

$$\langle \mu_L^z \rangle = 2\gamma^2 \Delta n/3, \tag{5.16}$$

$$\langle \mu_S^z \rangle = (4\gamma^2 - 3)\Delta n/3 \tag{5.17}$$

where Δn is the difference of the occupation numbers of $|\psi_{\pm 1/2}\rangle$.

Our calculations show that the $j_{\text{eff}} = 1/2$ band has dominant d_{yz} and d_{xz} characters [20], which stabilizes the superexchange interaction between the spins on Ir^{4+} ions and helps formation of the AFM order. It is thus demonstrated that the interplay of SOC and magnetic correlation both play important roles in the gap formation of $CaIrO_3$.

5.4 Results and discussions

We performed DFT+DMFT calculations for $CaIrO_3$ with AFM order at a series of temperatures: 464K, 232K, 203K, and 116K. The one-particle spectra are shown in Figure 5.5, Figure 5.6, Figure 5.7, and Figure 5.8. The spectral function for the insulating ground state at 116K is also presented in Figure 5.9, which can be directly compared to experiments if they are available. By observing the density of states, we can see that the gap formation happens around 230K. Above this temperature, it is paramagnetic metallic phase since the symmetry of spin-up and spin-down density of states of $5d$ projection. Below 230K, the $j_{\text{eff}} = 1/2$ begins to split into two bands,

and the symmetry between spin-up and spin-down is broken. In addition, the energy range around Fermi energy is dominated by Ir-5d orbitals, in which lies the interplay of cystal-field potential, magnetic correlation and electron correlation. The result states that the transition happens around 230K from paramagnetic metallic phase into AFM insulating phase, which can be further corroborated by the behavior of magnetic moments obtained through Eq. 5.16 and Eq. 5.17. The magnetic moments are shown in Figure 5.4. It can be seen that the magnetic moment increases sharply at the MIT temperature, indicating that the MIT is accompanied with the magnetic transition. The conclusion from DFT+DMFT calculations is also supported by resonant inelastic x-ray scattering (RIXS) [83], and DFT+SOC calculations [20].

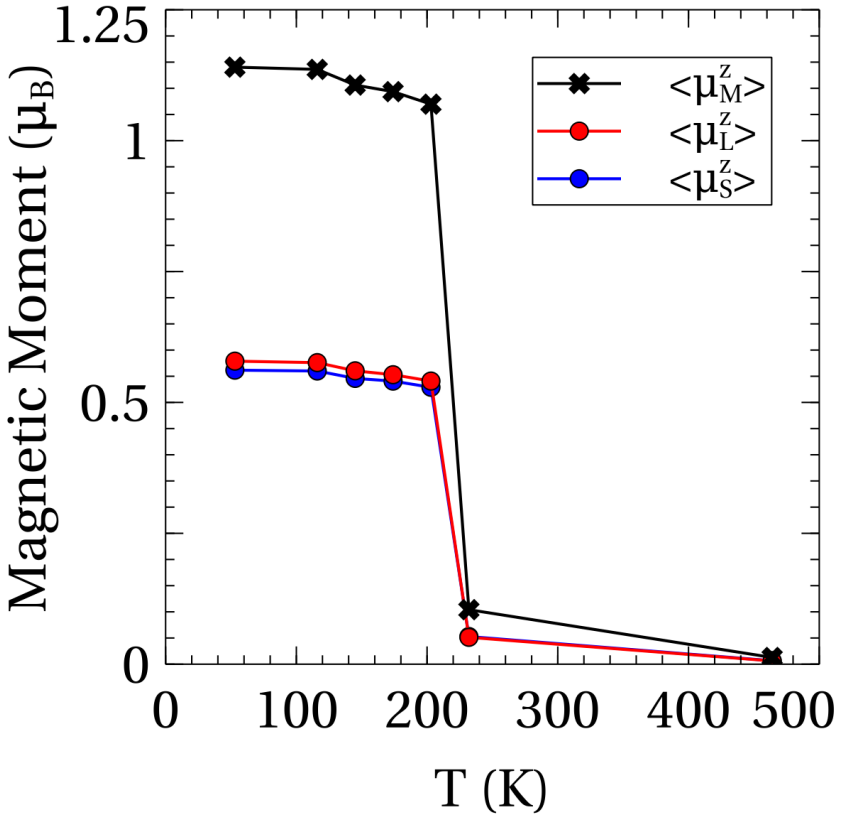

Figure 5.4: Magnetic momentum of Ir atom in $CaIrO_3$ as a function of temperature. Included are total, orbital, and spin magnetic moments.

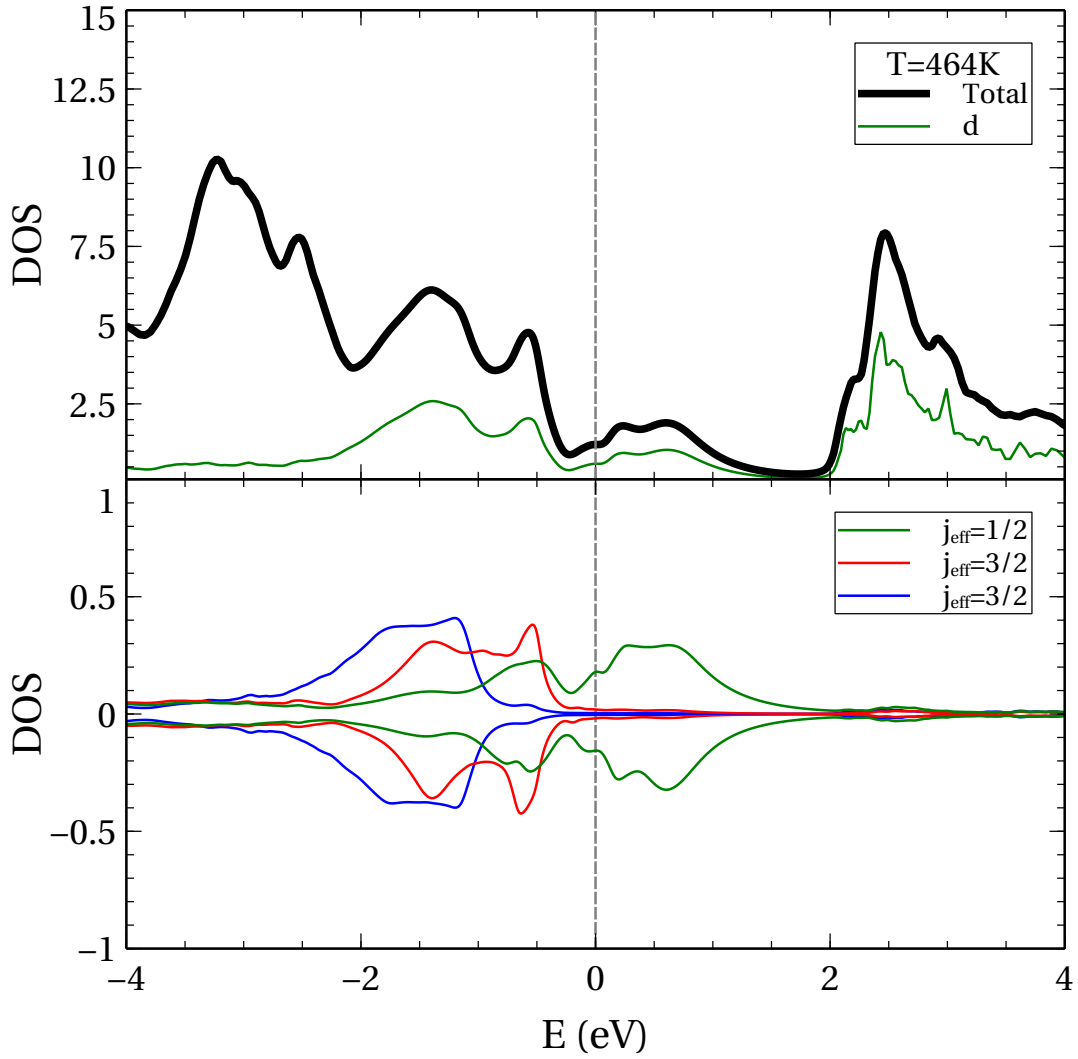

Figure 5.5: Density of states of $CaIrO_3$ at 464K obtained from DFT+DMFT calculations. The upper plot shows the total and partial-d density of states. The lower plot shows the spin-up and spin-down projected density of states for $j_{\text{eff}} = 1/2$ and $j_{\text{eff}} = 3/2$.

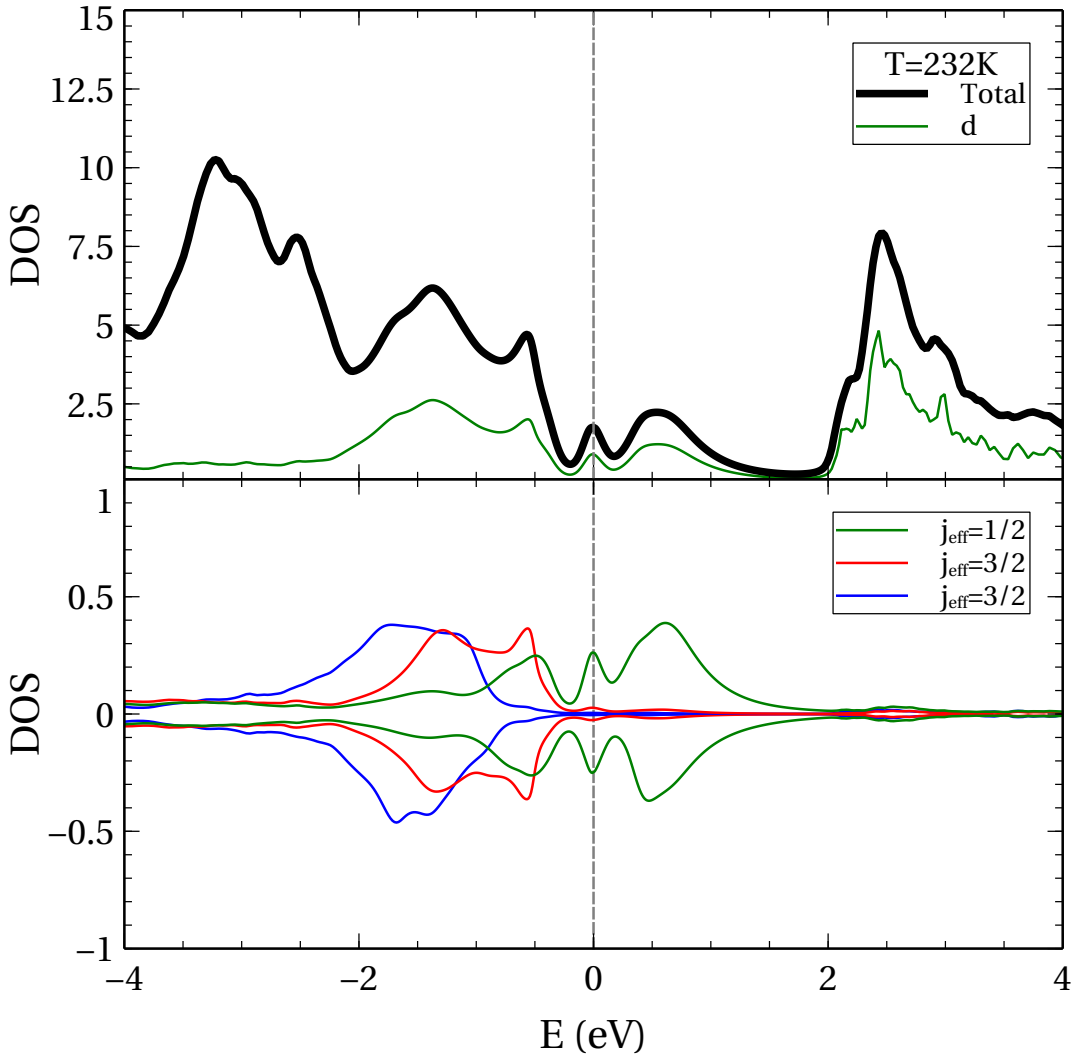

Figure 5.6: Density of states at 232K obtained from DFT+DMFT calculations. The upper plot shows the total and partial-d density of states. The lower plot shows the spin-up and spin-down projected density of states for $j_{\text{eff}} = 1/2$ and $j_{\text{eff}} = 3/2$.

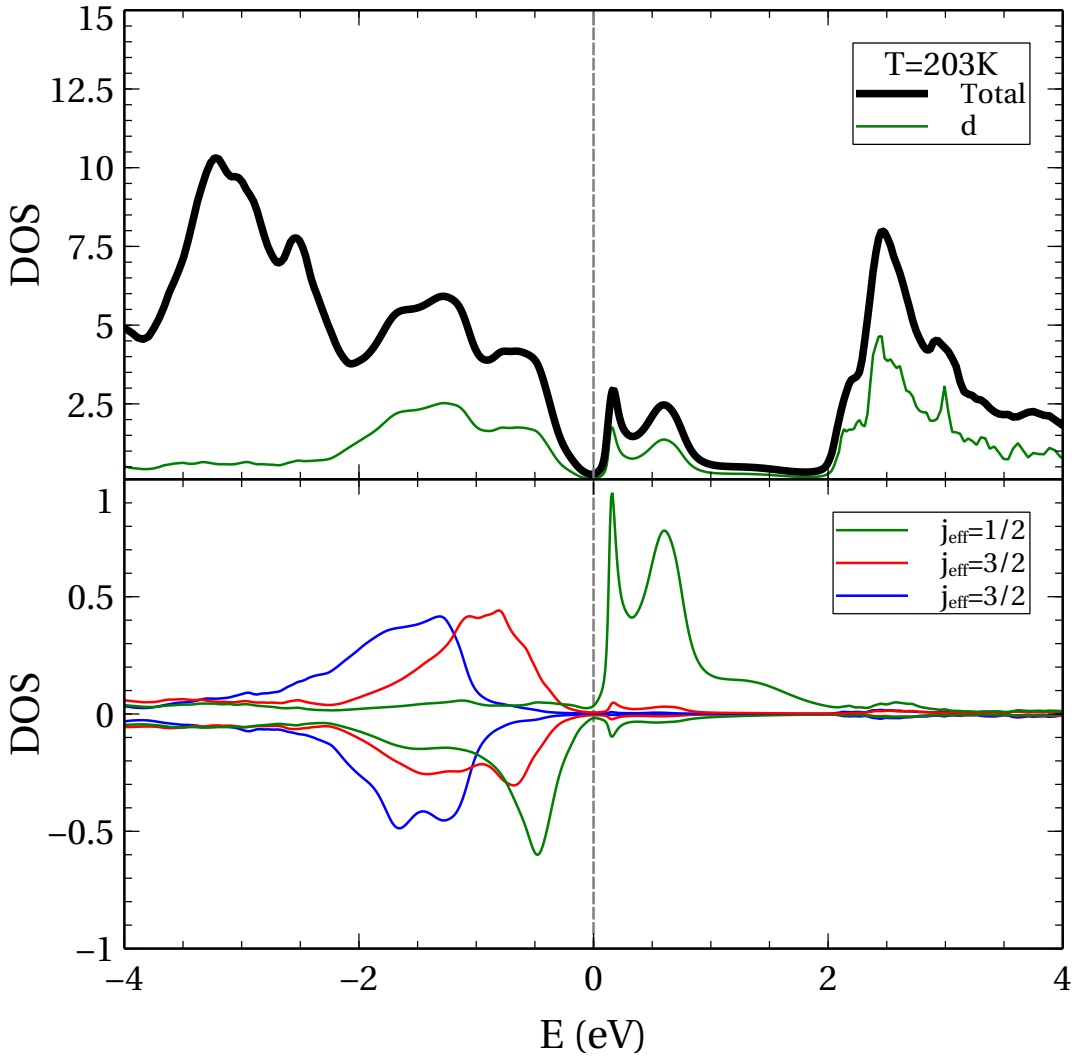

Figure 5.7: Density of states at 203K obtained from DFT+DMFT calculations. The upper plot shows the total and partial-d density of states. The lower plot shows the spin-up and spin-down projected density of states for $j_{\text{eff}} = 1/2$ and $j_{\text{eff}} = 3/2$.

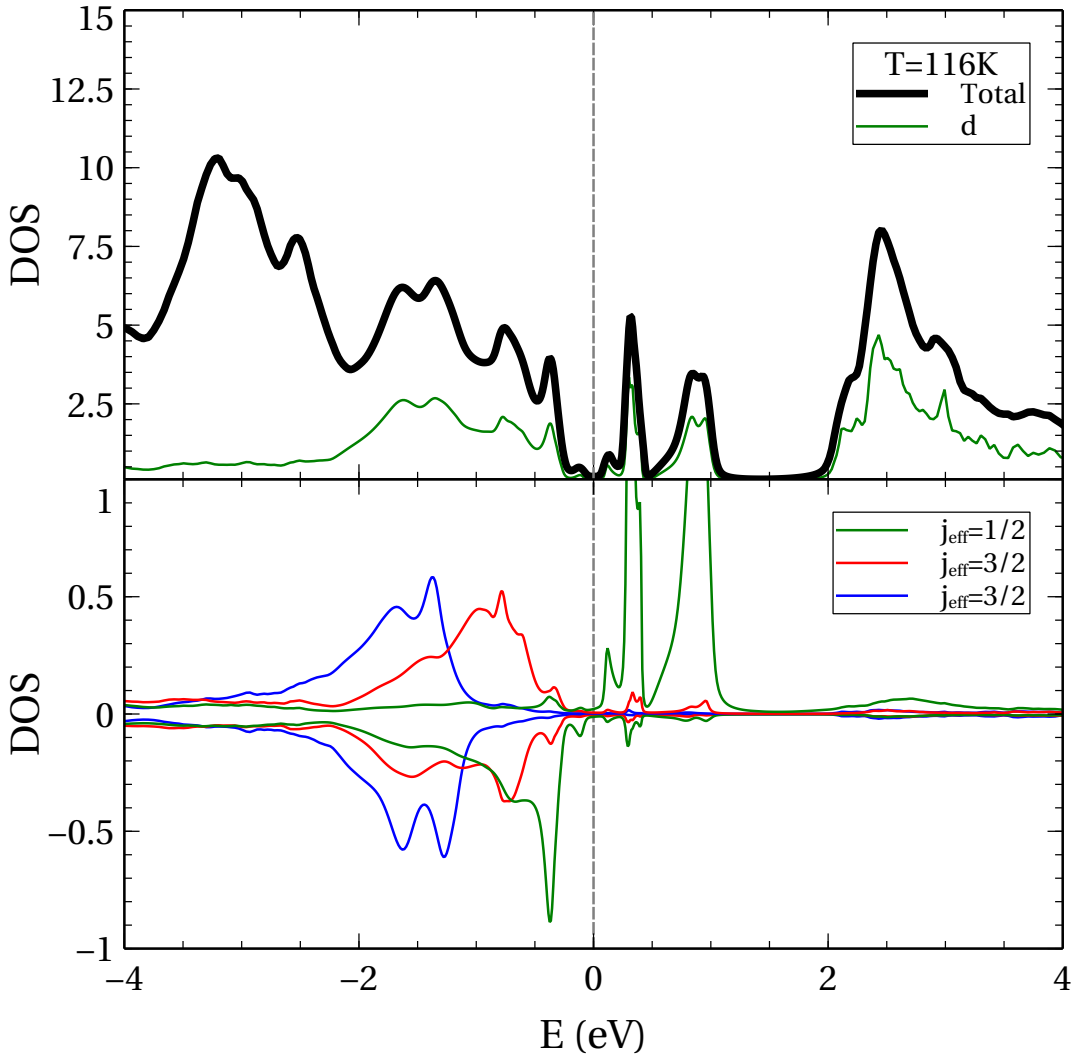

Figure 5.8: Density of states at 116K obtained from DFT+DMFT calculations. The upper plot shows the total and partial-d density of states. The lower plot shows the spin-up and spin-down projected density of states for $j_{\text{eff}} = 1/2$ and $j_{\text{eff}} = 3/2$.

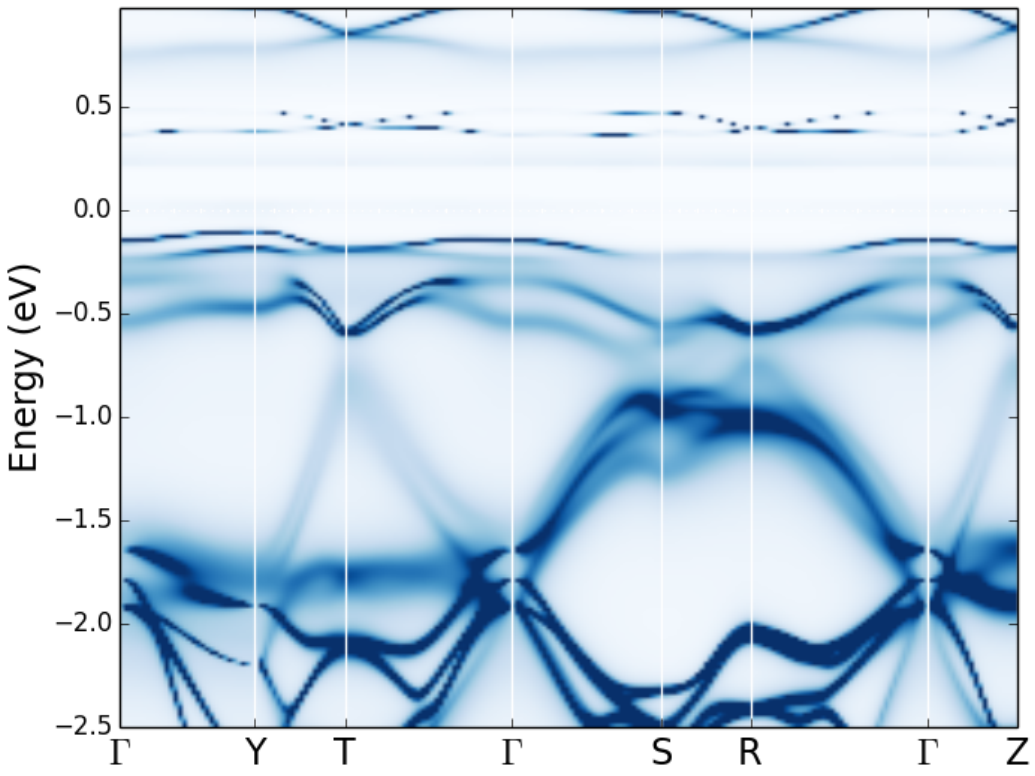

Figure 5.9: Band structure at 116K, obtained by DFT+DMFT calculations.

CHAPTER 6. CONCLUSION

In this thesis, we made two modifications into the existing CMR formalism in order to mitigate the errors introduced by the CMR approximations. We proposed a fixed form for the one-electron renormalization factor and included a sum-rule term into the CMR energy functional, which successfully shift major inter-site two-electron contribution to the local on-site interactions. The new CMR method has also proved to be reasonably close to exact results for a series of molecules including H_n clusters, homonuclear and heteronuclear molecules. This study will benefit our future development of the CMR method in bulk materials.

We also demonstrated the feasibility of calculating the MAE from the CCI method in electronic systems. For practical applications, we performed calculations on the total energies for Al, Pt and Pu crystals and the MAE for CoPt and FePt. The results also show satisfactory agreement with what are calculated from self-consistent calculations. By resolving the SOC energies and orbital magnetic moments into different atomic sites and spin-transition processes, we also found that the MAE is attributed predominantly to the majority spin conservation term at Pt site, giving us a better understanding of the microscopic origin of MAE.

We also employed the DFT+DMFT method to clarify the effects of tetragonal crystal field, AFM order and SOC on d orbitals of $CaIrO_3$. By investigating the density of states and magnetic moments at different temperature, we found that the insulating-gap formation is concomitant with the magnetic transition, indicating that the long range AFM order should also contribute to the open gap as well as the SOC. These calculations

indicate that $CaIrO_3$ should be classified into Slater insulator rather than Mott insulator. These findings change the understanding of MITs in Iridium oxides, in which compounds like Sr_2IrO_4 and Na_2IrO_3 that are previously proposed to be Mott-Hubbard insulators probably need further studies.

BIBLIOGRAPHY

[1] E.W. Lemmon, M.O. McLinden, D.G. Friend, P.J. Linstrom and W.G. Mallard, *NIST chemistry WebBook, Nist standard reference database number 69* (National Institute of Standards and Technology, Gaithersburg MD, 20899, Gaithersburg, 2016).

[2] B.D. Darwent, *Bond Dissociation Energies in Simple Molecules* (National Bureau of Standards, Washington D.C., 1970).

[3] K. P. Huber and G.Herzberg, *MOLECULAR SPECTRA and MOLECULAR STRUCTURE IV. CONSTANTS OF DIATOMIC MOLECULES* (Springer Science and Business Media, New York, 1979).

[4] E.A. Colbourn, M. Dagenais, A.E. Douglas and J.W. Raymonda, Canadian Journal of Physics **54** (13), 1343 (1976).

[5] T.H. Dunning, The Journal of Chemical Physics **65** (10), 3854 (1976).

[6] P.W. Anderson, Science (New York, N.Y.) **177** (4047), 393 (1972).

[7] P. Hohenberg and W. Kohn, Physical Review **136** (3B), B864 (1964).

[8] W. Kohn and L.J. Sham, Physical Review **140** (4A), A1133 (1965).

[9] Y.X. Yao, J. Liu, C.Z. Wang and K.M. Ho, Physical Review B **89** (4), 045131 (2014).

[10] Y.X. Yao, J. Liu, C. Liu, W.C. Lu, C.Z. Wang and K.M. Ho, Scientific reports **5**, 13478 (2015).

[11] C. Liu, J. Liu, Y.X. Yao, P. Wu, C.Z. Wang and K.M. Ho, Journal of Chemical Theory and Computation **12** (10), 4806 (2016).

[12] A. Georges, W. Krauth and M.J. Rozenberg, Reviews of Modern Physics **68** (1), 13 (1996).

[13] S.Y. Savrasov, G. Kotliar and E. Abrahams, Nature **410** (6830), 793 (2001).

[14] G. Kotliar, S.Y. Savrasov, K. Haule, V.S. Oudovenko, O. Parcollet and C.a. Marianetti, Reviews of Modern Physics **78** (3), 865 (2006).

[15] C.C.J. Roothaan, Reviews of Modern Physics **23** (2), 69 (1951).

[16] M.C. Gutzwiller, Physical Review **137** (6A), A1726 (1965).

[17] J. Bünemann, W. Weber and F. Gebhard, Physical Review B **57** (12), 6896 (1998).

[18] W.C. Lu, C.Z. Wang, M.W. Schmidt, L. Bytautas, K.M. Ho and K. Ruedenberg, Journal of Chemical Physics **120** (6), 2629 (2004).

[19] W.C. Lu, C.Z. Wang, M.W. Schmidt, L. Bytautas, K.M. Ho and K. Ruedenberg, The Journal of Chemical Physics **120** (6), 2638 (2004).

[20] S.W. Kim, C. Liu, H.J. Kim, J.H. Lee, Y. Yao, K.M. Ho and J.H. Cho, Phys. Rev. Lett. **115** (9), 96401 (2015).

[21] A. Szabo and N.S. Ostlund, *Modern quantum chemistry: introduction to advanced electronic structure theory* (McGraw-Hill, New York, 1989).

[22] W.J. Hehre, R.F. Stewart and J.A. Pople, The Journal of Chemical Physics **51** (6) (1969).

[23] J.S. Binkley, J.A. Pople and W.J. Hehre, Journal of the American Chemical Society **102** (3), 939 (1980).

[24] G.A. Petersson, A. Bennett, T.G. Tensfeldt, M.A. AlLaham, W.A. Shirley and J. Mantzaris, The Journal of Chemical Physics **89** (4) (1988).

[25] T.H. Dunning, The Journal of Chemical Physics **90** (2) (1989).

[26] J.C. Slater, Physical Review **51** (10), 846 (1937).

[27] J.C. Slater, Physical Review **81** (3), 385 (1951).

[28] D.J. Singh and L. Nordstrom, *Planewaves, Pseudopotentials, and the LAPW method* (Springer Science and Business Media, New York, 2006).

[29] S.R. White, Physical Review Letters **69** (19), 2863 (1992).

[30] G.K.L. Chan and S. Sharma, Annual Review of Physical Chemistry **62** (1), 465 (2011).

[31] S. Wouters and D. Neck, The European Physical Journal D **68** (9), 1 (2014).

[32] H. Zheng and L.K. Wagner, Physical Review Letters **114** (17), 176401 (2015).

[33] F. Ma, W. Purwanto, S. Zhang and H. Krakauer, Physical Review Letters **114** (22), 226401 (2015).

[34] N. Devaux, M. Casula, F. Decremps and S. Sorella, Physical Review B **91** (8), 81101 (2015).

[35] V.I. Anisimov, J. Zaanen and O.K. Andersen, Phys. Rev. B **44** (3), 943 (1991).

[36] V.I. Anisimov, F. Aryasetiawan and I. Lichtenstein, J. Phys.: Condens. Matter **9** (997), 767 (1997).

[37] K.M. Ho, J. Schmalian and C.Z. Wang, Physical Review B **77** (7), 073101 (2008).

[38] Y.X. Yao, C.Z. Wang and K.M. Ho, Physical Review B **83** (24), 245139 (2011).

[39] X.Y. Deng, L. Wang, X. Dai and Z. Fang, Physical Review B **79** (7), 75114 (2009).

[40] X. Deng, X. Dai and Z. Fang, EPL (Europhysics Letters) **83** (3), 37008 (2008).

[41] N. Lanatà, H.U.R. Strand, X. Dai and B. Hellsing, Physical Review B **85** (3), 35133 (2012).

[42] G. Wang, Y. Qian, G. Xu, X. Dai and Z. Fang, Physical Review Letters **104** (4), 47002 (2010).

[43] M.T. Czyżyk and G.A. Sawatzky, Physical Review B **49** (20), 14211 (1994).

[44] D.K. Seo, Physical Review B **76** (3), 33102 (2007).

[45] M. Karolak, G. Ulm, T. Wehling, V. Mazurenko, A. Poteryaev and A. Lichtenstein, Journal of Electron Spectroscopy and Related Phenomena **181** (1), 11 (2010).

[46] K. Haule, T. Birol and G. Kotliar, Physical Review B **90** (7), 75136 (2014).

[47] K. Haule, Physical Review Letters **115** (19), 196403 (2015).

[48] A.L. Fetter and J.D. Walecka, *Quantum theory of many-particle systems* (McGraw-Hill Book Company, New York, 1971).

[49] J. Bünemann and F. Gebhard, Physical Review B **76** (19), 193104 (2007).

[50] N. Lanatà, Y.X. Yao, C.Z. Wang, K.M. Ho and G. Kotliar, Physical Review X **5** (1), 11008 (2015).

[51] R. Krishnan, J.S. Binkley, R. Seeger and J.A. Pople, The Journal of Chemical Physics **72** (1) (1980).

[52] L. Bytautas, N. Matsunaga, T. Nagata, M.S. Gordon and K. Ruedenberg, The Journal of chemical physics **127** (20), 204301 (2007).

[53] L. Hedin, Phys. Rev. **139** (3A), A796 (1965).

[54] M. Van Schilfgaarde, T. Kotani and S. Faleev, Phys. Rev. Lett. **96** (22), 226402 (2006).

[55] T. Kotani, M. van Schilfgaarde and S.V. Faleev, Phys. Rev. B **76** (16), 165106 (2007).

[56] J. Harris and R.O. Jones, Journal of Physics F: Metal Physics **4** (8), 1170 (1974).

[57] D. Langreth and J. Perdew, Solid State Communications **17** (11), 1425 (1975).

[58] O. Gunnarsson and B. Lundqvist, Physical Review B **13** (10), 4274 (1976).

[59] J. Perdew, D. Langreth and V. Sahni, Physical Review Letters **38** (18), 1030 (1977).

[60] P. Bruno, Magnetismus von Festkörpern und grenzflächen **24**, 1 (1993).

[61] J.H. van Vleck, Physical Review **52** (11), 1178 (1937).

[62] D.D. Koelling and B.N. Harmon, Journal of Physics C: Solid State Physics **10** (16), 3107 (1977).

[63] P. Blaha, K. Schwarz, G.K.H. Madsen, D. Kvasnicka and J. Luitz, *WIEN2K. An augmented plane wave+ local orbitals program for calculating crystal properties* (Technische Universitat Wien, Vienna, 2001).

[64] K. Buschow, P. van Engen and R. Jongebreur, Journal of Magnetism and Magnetic Materials **38** (1), 1 (1983).

[65] P. Ravindran, A. Kjekshus, H. Fjellvåg, P. James, L. Nordström, B. Johansson and O. Eriksson, Physical Review B **63** (14), 144409 (2001).

[66] A. Sakuma, Journal of the Physical Society of Japan **63** (8), 3053 (1994).

[67] V. Antropov, L. Ke and D. Åberg, Solid State Communications **194**, 35 (2014).

[68] P. Bruno, Physical Review B **39** (1), 865 (1989).

[69] Y. Kota and A. Sakuma, Journal of the Physical Society of Japan **81** (8), 84705 (2012).

[70] B.J. Kim, H. Jin, S.J. Moon, J.Y. Kim, B.G. Park, C.S. Leem, J. Yu, T.W. Noh, C. Kim, S.J. Oh, J.H. Park, V. Durairaj, G. Cao and E. Rotenberg, Physical Review Letters **101** (7), 76402 (2008).

[71] B.J. Kim, H. Ohsumi, T. Komesu, S. Sakai, T. Morita, H. Takagi and T. Arima, Science (New York, N.Y.) **323** (5919), 1329 (2009).

[72] R. Arita, J. Kune, a.V. Kozhevnikov, a.G. Eguiluz and M. Imada, Physical Review Letters **108** (February), 1 (2012).

[73] M. Moretti Sala, M. Rossi, S. Boseggia, J. Akimitsu, N.B. Brookes, M. Isobe, M. Minola, H. Okabe, H.M. Rønnow, L. Simonelli, D.F. McMorrow and G. Monaco, Physical Review B **89** (12), 121101 (2014).

[74] K. Ohgushi, J.I. Yamaura, H. Ohsumi, K. Sugimoto, S. Takeshita, A. Tokuda, H. Takagi, M. Takata and T.H. Arima, Physical Review Letters **110** (21), 1 (2013).

[75] M.M. Sala, K. Ohgushi, A. Al-Zein, Y. Hirata, G. Monaco and M. Krisch, Physical Review Letters **112** (17), 176402 (2014).

[76] N. Blümer, Ph.D. thesis, der Universität Augsburg 2003.

[77] K. Haule, C.H. Yee and K. Kim, Physical Review B **81** (19), 195107 (2010).

[78] J.P. Perdew, K. Burke and M. Ernzerhof, Physical Review Letters **77** (18), 3865 (1996).

[79] P. Werner, A. Comanac, L. de' Medici, M. Troyer and A.J. Millis, Physical Review Letters **97** (7), 76405 (2006).

[80] K. Haule, Physical Review B **75** (15), 155113 (2007).

[81] H. Zhang, K. Haule and D. Vanderbilt, Physical Review Letters **111** (24), 246402 (2013).

[82] A. Kutepov, K. Haule, S.Y. Savrasov and G. Kotliar, Physical Review B **82** (4), 45105 (2010).

[83] M.M. Sala, K. Ohgushi, A. Al-Zein, Y. Hirata, G. Monaco and M. Krisch, Physical Review Letters **112** (17), 176402 (2014).